

# **Supporting Information: Data Analysis and Model Construction Procedures**

for paper

## **Segmentation of Plate Coupling, Fate of Subduction Fluids, And Modes of Arc Magmatism in Cascadia, Inferred from Magnetotelluric Resistivity**

*Wannamaker, P. E., R. L. Evans, P. A. Bedrosian,  
M. J. Unsworth, V. Maris and R S. McGary*

**Geochemistry, Geophysics, Geosystems**  
**American Geophysical Union**

Here we discuss characteristics and modelling of the Cascadia MT data sets in sufficient detail to substantiate the resistivity cross sections described in the main text. Summary data representations, geoelectric strike estimates, and individual site examples of the data are plotted. Responses of the models are compared to the data for goodness of fit. A brief description of the inversion algorithms are presented.

### **S1. Magnetotelluric Method**

The MT electromagnetic (EM) geophysical method has been reviewed thoroughly elsewhere [Vozoff, 1991; Simpson and Bahr, 2005; Chave and Jones, 2012]. The exploited signals for wave periods shorter than  $\sim 1$  s originate from regional and global lightning activity propagating along the earth-ionosphere waveguide. Signals at longer periods originate from solar wind-magnetospheric interactions and can be obtained to as great as 20,000 s and sometimes more. Measured time series are decomposed into separate frequencies usually using cascade decimation, and auto- and cross-power spectra estimated to form the 2x2 tensor impedance and 1x2 tensor vertical magnetic field transfer function (tipper).

Because of the remoteness of the sources and the high index of refraction of the Earth relative to air, the incident EM waves are treated as planar fronts propagating vertically into the ground. Robust outlier removal methods have been developed to remove data subsets that do not meet that assumption. Electrical conduction dominates over dielectric displacement in the Earth, so MT wave propagation in the subsurface is diffusive. Thus, methods to produce electrical resistivity images of the subsurface from MT data require stabilized or regularized inversion methods which simultaneously attempt to fit the data and suppress model artifacts [Tarantola, 1987; Zhdanov, 2002; Chave and Jones, 2012].

### **S2. Field Data Collection**

The four U.S. profiles utilized two styles of instruments. The first are so-called wideband (WB) devices measuring in the wave period range 0.005 through 500 s typically. Magnetic fields

of the MT signals are recorded using sensitive solenoids while electric fields are obtained as voltage differences across bipoles grounded with quiet chemical electrodes. Natural signals tend to be weak in the so-called dead band from  $\sim 0.2 - 10$  s, and this was especially true during the solar activity minimum of 2009-2010. The CAFE and Klamath-Modoc WB data were acquired under commercial contract using L-array bipoles and involved typical recording times of 15 hours per site. To avoid noise biases especially in the dead band, the CAFE and Klamath-Modoc wideband data were recorded with a simultaneous ultra remote reference in western Nevada. An exception for Klamath-Modoc was the three westernmost WB sites on the Eel River delta, recorded using Schlumberger MT24 LF instruments with a remote reference 80 km to the east. The SWORMT profile was acquired using up to four simultaneously recording MT24 LFs separated by up to 50 km.

The contracted time series were processed using robust outlier removal in both frequency and time domain following methods described by Larson and by Egbert [*Chave and Jones, 2012*]. The Klamath-Modoc WB data generally are excellent, and mostly very good for CAFE, although with the solar minimum high quality could be a challenge through urbanized Olympia and Puyallup areas near the CAFE profile center. The SWORMT wideband data were processed to response functions using the robust, multi-station transfer function estimation program of *Egbert (1997)*. The older EMSLAB data were acquired by now defunct university systems of four different types; response parity was checked in a separate pre-experiment in central Oregon [*Young et al., 1988*]. These utilized only local or cross-site referencing with coherency sorting which did not achieve complete noise reduction for several sites in the MT dead band (1-10 s) across the central developed Willamette Valley. However, this band is not of primary pertinence for the main structures interpreted herein.

The second style of instrument is the long period (LP) device which is somewhat similar in design but is meant to consume less power and measure unattended for 3-6 weeks (so-called NIMS recorders). Because induction coils typically lose sensitivity for periods greater than several hundred seconds, fluxgate magnetometers are used for long periods. Lateral variation in the frequency dependence of the MT response becomes smoother toward longer periods, so fewer LP recording are needed relative to the WB. In the case of the contracted WB data taken first, the LP sites were placed as close as possible to corresponding WB sites, but some variance (few 100 m) was typical due to access and security. The SWORMT LP data were recorded simultaneously with its WB data using the same electric field bipoles. Time series were processed to response functions using the multi-site robust outlier removal program of *Egbert [1997]*. For the British Columbia (ABCS) profile, only LP data were acquired using a mix of older recorders such as used in EMSLAB and newer NIMS as used in CAFE, SWORMT and Klamath-Modoc [*Soyer and Unsworth, 2006; Rippe et al., 2013*].

The WB and LP soundings of the CAFE, EMSLAB and Klamath-Modoc lines were merged for pseudosection display and 2D inversion. First, following rotation of all soundings to a uniform coordinate system based upon geoelectric strike estimates described shortly, the LP apparent resistivities were static shifted to the amplitude levels of the WB apparent resistivities using the  $\sim 1.5$  decade period range of overlap ( $\sim 20$  to 600 s). Both WB and LP data generally were of good quality in this overlap and so the data were binned into common period points using a Gaussian error weighting. This binning procedure was applied also to the EMSLAB WB data set, coming as it did from four different instrument types. Next, values from neighboring pairs of LP soundings were linearly interpolated to locations of intervening WB soundings and apparent resistivities again static shifted to the WB levels. These interpolated LP values were not

used in the inversions, but only for ease of graphical display in contour plots. The x-axis is assigned to geographical north and the y-axis is geographical east for all sites and all periods in the upcoming pseudosections except for ABCS. We will show that this x-axis is compatible with regional geoelectric strike for the purpose of 2D inversion. The ABCS x-axis was N030W as used by *Soyer and Unsworth* [2006]. The MT24 LF instruments on the SWORMT profile utilized the same electric field bipole setups as installed for the NIMS, so precisely coincident recordings were made thus avoiding static differences between WB and LP.

### S3. CAFE Profile Analysis

#### S3.1 Observed Data

Our measured results most pertinent to model construction are summarized in Fig. S1 as pseudosections, where log period (T, in s) serves as ordinate and horizontal distance as abscissa for contour plots of MT response amplitude [*Vozoff, 1991*]. The period range of 0.008 to 10000 s is sampled at 42 logarithmically spaced points. The results are presented for an x-axis (assumed strike) of N000E for all sites and all periods, parallel to large-scale geology and consistent with MT strikes presented later. The upper two panels show apparent resistivity and impedance phase ( $\rho_{yx}$  and  $\phi_{yx}$ ), which correspond nominally to electric current flow across strike. This would be the transverse magnetic (TM) mode [*Vozoff, 1991*] in a 2D geometry. The lower panel shows the real part of the normalized vertical field primarily due to cross-strike variations of along-strike current flow ( $\text{Re}(K_{zy})$ ). Nominally, these are data of the transverse electric (TE) mode. As we describe, these three panels represent the subset of the total MT response which is more robust in the 2D assumption for model construction. Ascribed structural features below are listed in light of the 2D inversion model construction experience.

Low values of  $\rho_{yx}$  are seen for the upper two-thirds of the period range in the western 60 km of the transect over shallow former marine sediments and possibly subsurface accreted trench sediments (Figure S1a). Higher  $\rho_{yx}$  eastward to profile center is coincident with Siletz terrane igneous rocks and, at greater depth, lower crust and upper mantle. Just west of Mount Rainier, a narrow pair of low  $\rho_{yx}$  lobes extends from middle to long period with high  $\rho_{yx}$  from Rainier eastward ~50 km. Low values of  $\rho_{yx}$  characterize the eastern reaches of the profile due to altered Tertiary volcanic flows over metamorphic basement of the Manastash Ridge and Wenachie highlands. As is characteristic of the nominal TM mode data, apparent resistivity pseudosection contours prolong vertically to long periods due to the effect of boundary electric charges along sides of structures [e.g., *Wannamaker, 1999*].

It is in  $\phi_{yx}$  that the diagnostic responses of important structures are most apparent (Figure S1b). Moving from west to east, warm colors at relatively short periods denote the accreted middle Cenozoic trench sediments, the Puget Lowlands basin, and altered Miocene and younger volcanics of the backarc highlands. Under the western half of the profile, very low  $\phi_{yx}$  values (cool colors) in the 100-2000 s period range indicate high resistivities of the subducting Juan de Fuca plate. Warm colors ( $\phi_{yx}$  values >45 degrees) at these longer periods over the eastern half, which in fact move to yet longer periods to the far east, suggest a deep conductor dipping eastward. In the center at middle period lies a tight, bilobate high phase zone corresponding to similar low  $\rho_{yx}$  cited previously indicating a compact steep conductor just west of Mount Rainier.

Information content about the deepening conductor along the plate interface and its subsequent migration to lower, and then middle, crustal levels as the arc is approached is contained in

the subtle peak in  $\phi_{yx}$  in the 10-100 s period range below the western half of the profile (Figure S1b). This peak is weaker and lies at somewhat longer periods  $\sim 75$  km from the coast relative to 25 km from the coast, and then becomes stronger and moves to shorter periods 100-150 km inland. However, note that the peak is entirely absent under the 3-4 sites immediately adjacent to the coast. These are the data, examined later in a sensitivity test, indicating lack of a plate interface conductor under the coastline and westward.

Quantity  $K_{zy}$  is sensitive to lateral variations in electric current flow parallel to assumed strike and thus provides information about along-strike structural continuity (Figure S1c). Only the real component is plotted as it is more physically intuitive to examine. A modest high in  $\text{Re}(K_{zy})$  is seen in the 100-10000 s range for the four sites nearest the coast which in part denotes presence of the conductive seawater laterally. The high region in the 40-70 km inland range extending to somewhat shorter periods in large part is due to the compact conductor above the plate interface that was judged to be a package of middle Cenozoic trench sediments abutting Siletzia. The most striking feature is the strong cross-over anomaly near profile center occupying much of the period range. As modelling shows, this is due to the steep, strong conductor starting within a few kilometers of the surface just west of Mount Rainier and dipping steeply east toward the plate interface. The modest positive in over the 100-10000 s range extending to the east end of the profile is evidence for a yet deeper conductor to the east which will correspond to the BA1 upwelling of *Megbel et al.* [2014] and the deep model conductor of Figure 2 of the main text.

The nominal TE mode impedance quantities  $\rho_{xy}$  and  $\phi_{xy}$  are shown in the upper two panels of Figure S2a-b while the normalized vertical magnetic field reflecting along-strike changes in cross-strike current flow ( $\text{Re}(K_{zx})$ ) is in the lower panel (Figure S2c). We see  $\rho_{xy}$  typically is of much lower amplitude near the coast than the TM  $\rho_{yx}$ , due in large part to presence of the flanking seawater. This obscures presence of the resistive plate below. Numerous static shifts along the profile persisting to the longest periods are apparent in  $\rho_{xy}$  also, which should not appear if this quantity is behaving 2D. One prominent feature of note is the very low  $\rho_{xy}$  and high  $\phi_{xy}$  under Mount Rainier and immediately east. This is a response to the apparent very low resistivities at lower crustal and shallow upper mantle depths inferred from the TM mode and seen in main text Figure 2, but we will argue with the model construction section that 3D effects exist in the nominal TE mode which make its formal inclusion hazardous in the inversion.

The vertical magnetic field quantity  $K_{zx}$  in Figure S2c shows that there are a few features offline violating a strict 2D assumption but these are not considered serious. A compact positive anomaly in the 10-100 s range  $\sim 20$  km from the coast means there is a conductor lying some distance south of the profile here. Negative values in the 2-200 s range near profile center suggest higher conductivity to the north which may be associated with the Puget Lowlands and Sound [cf. *Apraia et al.*, 1998]. Negative values at short periods just east of Mount Rainier denote a shallow ( $\sim 1$  km) conductor to the north of unknown origin. A weak positive in the 100-10000 s range under the eastern portion of the profile indicates that strike of the deep BA1 conductor is somewhat east of north given our data sign conventions. We will discuss the ramifications of such irregularities in  $K_{zx}$  and how they are treated in 2D modelling.

### S3.2 Geoelectric Trend Estimation

An important issue in MT is the ability to estimate deeper structural trends in the face of distorting influence by shallower resistivity heterogeneity. The assumed geoelectric strike of N000E based largely on observed regional tectonics is tested for CAFE against principal axes of

the impedance phase tensor [Caldwell *et al.*, 2004; Booker, 2013] (Figure S3). This is done for a nominal forearc and a backarc area by dividing the profile precisely in two, and for three period bands corresponding to sensitivity depth ranges from the upper middle crust to >200 km.

The majority of the rose histograms show peaks which approximate north, allowing for the 90° ambiguity in impedance, consistent with the analysis of McGary *et al.* [2014]. There is some indeterminacy over the forearc area at the shortest period band where phase anisotropy is not strong. Over the arc and backarc at the shortest periods, the axes are somewhat east of north for reasons unclear, and there is some indeterminacy at middle periods. However, as a closer test of the Klamath-Modoc profile will show, such variations in strike are unlikely to be serious in the derivation of a model cross section.

Trends of phase tensor axes are reasonably compatible with the vertical magnetic field functions as seen in Figures S1 and S2. The stronger anomalies in  $K_{zy}$  relative to  $K_{zx}$  over the coastal area are consistent with the coastline and trench structure, and also the main contact between accreted sediments and Siletzia. The very strong anomaly just west of Mount Rainier is predominantly in  $K_{zy}$  although there is some deviation at the shortest periods and Puget sediments or seawater may be noticeable at mid periods at profile center. The deep eastern conductor strike is somewhat northeasterly but this still makes fixed angle inversion permissible as we will explain.

### S3.3 Starting Model and A Priori Constraints

The inversion code applied is essentially that which we have used recently elsewhere [Wannamaker *et al.*, 2008, 2009]. It is a streamlined implementation similar to the Occam-2 approach [deGroot-Hedlin and Constable, 1990]. It uses our in-house finite element forward and Jacobian engines [Wannamaker *et al.*, 1987; deLugao and Wannamaker, 1996], and the standard explicit iterative parameter step equation [Tarantola, 1987; Mackie *et al.*, 1988] where model slope is damped relative to that of an a priori model.

The CAFE forward mesh is 419 x 71 nodes (including 10 air layers) extending to ~10,000 km each side of the profile and to total depth of 1160 km, and terminates at each side in continental material (i.e. Pacific ocean width is finite). There are four element columns per MT station increasing in thickness geometrically downward from 25 m at the surface, although six columns per site were used around the rapidly varying anomalies just west of Mount Rainier. Two parameter columns per station are used, one under and one between each site, to a depth of 860 km and to within one finite element of each side of the mesh, for a total of ~8100 parameters.

We advocate using a starting model whose resistivity values represent some average of the observed data to minimize bias. Thus, as is our common practice [Wannamaker *et al.*, 2008, 2009], an integrated TM mode impedance sounding is generated which is roughly equivalent to measuring with one electric bipole in the y-direction of equal length to the entire transect [Torres-Verdin and Bostick, 1992]. A smooth 1D inversion of this sounding is performed which yielded values near 100 ohm-m at the surface, falling to a few tens at a few km depth, then rising again to 100 ohm-m and beyond toward greater depth. We do not allow the deeper values in the starting model to exceed 100 ohm-m at depth because the inflationary effect of the large seawater body is not taken into account in the integration. The starting (and a priori) model is shown in Figure S4. We only show the a priori model and its responses for CAFE as those for EMSLAB, Klamath-Modoc and ABCS are constructed similarly.

The computed responses of the a priori model are shown in Figure S5 and show primarily the effects of the land-sea transition. At longer periods, one sees an increase in  $\rho_{yx}$  and decrease in

$\phi_{yx}$  progressively stronger toward the coast. This is the effect of excess electrical current induced in the seawater and marine sediments being driven onto the land in the TM mode. At shorter periods, one sees the mild decrease in  $\rho_{yx}$  and increase in  $\phi_{yx}$  all along the land profile as an average shallow sedimentary section exists in the a priori model. The vertical magnetic field is included in this figure as it is inverted with the TM data. A strong positive in  $\text{Re}(K_{zy})$  occurs toward long periods near the coast, decaying with distance inland. For the TE mode impedance, the effect of the ocean structure is minor and confined to be within 50 km of the coast.

### S3.4 2D Inversion Model Construction

Despite the overall tectonic grain of the Pacific Northwest region, care must be exercised in applying 2D modelling approaches to a data set wherein departures from that assumption undoubtedly lie. Numerous 3D model studies confirm that 2D inversion of the nominal TM (yx) mode data over a structure varying along strike usually yields reasonably accurate cross-sections, especially for conductive structures [Wannamaker, 1999; Ledo, 2005; Siripunvaraporn *et al.*, 2005]. Viability of TM models stems from inclusion of boundary charge effects caused by current flow along resistivity gradients in both 2D and 3D formulations. An additional advantage not often recognized, the mean effect of shallower structure is compensated in the TM mode, removing bias in the recovery of larger-scale resistivities and geometry [Torres-Verdin and Bostick, 1992; Wannamaker, 1999]. Furthermore, although the principal axes of impedance and vertical magnetic field (and by inference phase tensor axes also) swing through 180 degrees along an off-axis profile over the synthetic basin model studied by Wannamaker [1999], those same studies showed that accurate cross sections through the basin could be obtained through fixed-axis 2D TM modeling. Finally, large-scale lateral conductors such as the seawater generate TM vertical current channeling effects which may enhance resolution of large-scale fault zones such as concern us in this project [Wannamaker *et al.*, 2002, 2008]. Tremor streaks resolved seismically by Ghosh *et al.* [2012] in northern Cascadia align primarily downdip of the subducting plate so this is expected to be the higher conductivity direction (TM mode) for resolving fluids there [cf. Wannamaker *et al.*, 2002].

On the other hand, boundary charge effects are not included in TE formulations so the effects of along-strike variations are fundamentally underrepresented in the physics of this mode [Wannamaker, 1999]. The static effects in Fig. S2 are one example of this, but they can exist at a variety of scales. Thus, we de-emphasize the TE impedance in model construction. Of the TE quantities,  $K_{zy}$  is more robust to along-strike changes because current flow at least is continuous and represents an average resistance along the flow path. Hence, we include this TE quantity in our inversion to help verify inferences from the TM data. In areas where  $K_z$  suggests strike is tilted, the projection of its values onto the strike direction has been seen as a good approximation for deriving cross sections [Chen *et al.*, 1993; Dosso *et al.*, 1996; Wannamaker *et al.*, 2009]. Nevertheless, at the end we return to the TE impedance data and show that our final model exhibits overall compatibility with them also.

Hence, the inverted quantities are the nominal TM mode  $\log_{10}(\rho_{yx})$  and  $\phi_{yx}$ , and  $\text{Re}(K_{zy})$  over the 42 periods. A handful of low TE mode  $\phi_{xy}$  values at middle short periods under the Puget Lowlands were included to help focus the base of the shallow sediments there. Total data set comprised  $\sim 3960$  data points, for the 2D distribution of  $\log_{10}(\rho)$  [cf. Hohmann and Raiche, 1988]. Error floors of 3  $\log_{10}$  %, 2 deg, and 0.04 were applied to apparent resistivity, phase and  $K_{zy}$  respectively, which are  $\sim 3/4$  of those used by McGary *et al.* [2014]. Floors one-half of those amplitudes were applied to the long-period (LP) data due to their greater accuracy and sparser number.

We also did not invert  $\text{Re}(K_{zy})$  for periods shorter than 0.1 s to reduce near-surface discretization demands.

Instead of sweeping through a series of roughness damping factors at each iteration, one value is selected at the outset whereby the square norm of the roughening matrix is a fraction (typically 0.2) of the norm of the error-weighted parameter sensitivity matrix, adjusted each iteration. We find this achieves a good fit with apparently stable models in a small number of iterations ( $\sim 10$  usually). Starting normalized root-mean-square (nRMS) for the CAFE data set was 17.6 while final nRMS misfit was 1.78. Trial runs with a range of damping factors 0.1-0.5 were done on final models to ensure the persistence of important areas of structure and to establish that we were near the knee of the L-curve of misfit, similar to other studies [Booker *et al.*, 2004]. Models were run on a 3.4 GHz desktop Pentium PC and took  $\sim 4$  hours of runtime.

We did not constrain the inversion to require all low resistivity material to form above the estimated slab surface [cf. McGary *et al.*, 2014] for any of our three profiles. The slab becomes increasingly poorly constrained as the arc is approached and we wished to show what the MT data alone could resolve in this study. We believe there are numerous strong inferences possible with the models constructed as they are.

### S3.5 Computed Model Responses

The computed model response pseudosections for the primary data included in the inversion are plotted in Figure S1d-f for comparison to the data. Qualitatively the fit is very good, replicating the main diagnostic features described previously. Note that the  $\phi_{yx}$  response peak of the conductive layer along the plate interface and rising to the crust toward the arc is absent for the few sites adjacent to the coast. One confined area of misfit is right at the coast at the longest periods where the computed amplitude of  $\text{Re}(K_{zy})$  is somewhat greater than observed. We can only speculate that current channelling from the large conductive body of exhumed trench sediments to the north under the Olympic Mountains [Aprea *et al.*, 1998] may be feeding through the lesser body of such sediments resolved under this profile and is over-counteracting the seacoast magnetic field effect. The  $\text{Re}(K_{zy})$  also is slightly underfit at longer periods directly under Mount Rainier. Some underfit is expected in such inversions given that there is a conservative error floor and the process is meant to jointly minimize data misfit and model roughness. Tighter fitting here likely would accentuate further the steep conductor under the projection of Mount Rainier extending to slab depths.

The computed TE impedance responses for our inversion model are plotted in Figure S2d-f. Even though we did not explicitly include all but a handful of these data in the inversion because of concerns over 3D effects, the model response and those data appear basically compatible given the expected 2D limitations. A strong positive in  $\phi_{xy}$  is seen under Mount Rainier area over a broad middle period range dipping toward the backarc. However, this anomaly does not extend to arbitrarily long periods as observed. Correspondingly, very low values of  $\rho_{xy}$  do not extend to arbitrarily long periods either but show a minimum at middle to long periods. This is classic 2D TE behavior for a conductor where no boundary charges are in the formulation and anomalies are band limited. We conclude that the longest period behavior in the data is a 3D effect involving finite strike or structural twist which requires 3D data coverage to constrain. Other features of the response which qualitatively appear in the data include the smaller positives in  $\phi_{xy}$  at  $\sim 80$  and 140 km inland associated with the deep crustal fluid-release conductor. However, there are several other static shift-like features in the observed  $\rho_{xy}$  that are not (cannot be) reproduced in the calculations.

### **S3.6 Test of Subduction Conductance under Coast**

The inversion model of main text Figure 2 showed essentially no increase in conductivity at plate interface depths under the coast or seaward relative to the 100 ohm-m starting model. This had implications for plate coupling in the northern Cascadia segment. We test the robustness of this model feature by imposing a thin conductive layer along the interface and computing the change in response (Figure S6 and S7). One sees that such a layer creates a peak in  $\phi_{yx}$  and a depression in  $\rho_{yx}$  for the response by the coast. The alternative computed trends clearly lie outside the data compared to the preferred model of Figure 2. For the four sites near the coast, the 12 ohm-m layer caused the nRMS to go from 2.05 to 3.21, and this change undoubtedly would have been more severe if we considered just the period band affected by this structure. The test layer conductances are small compared to that of the structure resolved under the EMSLAB line discussed next. On this basis, we reject the likelihood of significant sediments or their dewatering to a degree like that we will imply at northern Oregon latitudes.

### **S3.7 Test of Conductance of Subducted Oceanic Crust at Near-Forearc Depths**

A coherent, arcward dipping low S-wave velocity layer, often assigned to the subducted oceanic crust, disappears at a depth near 40 km under the CAFÉ line near the forearc-mantle corner (see main text). This is approximately at the onset of increased conductivity and is interpreted to represent the beginning of oceanic crustal eclogitization and other hydrous mineral breakdown. In the inversion model of Figure 2, the oceanic crust appears to become resistive farther inland at toward greater depths, whereas the liberated fluids appear to migrate upward into the upper plate crust. To test that the deeper resistive oceanic crust does not appear so merely because of poor resolution due to the crustal conductor, a thin low-resistivity layer is imposed on the Figure 2 model along the deeper oceanic crust until it reaches the main flux melting zone beneath Mount Rainier (Figure S8). The conductance of the layer is similar to that of the low resistivity fluidized crustal layer. The forward response of this altered model at a diagnostic MT site (28 from the coast) is compared in Figure S9 with the TM (yx) mode response of the preferred model of Figure 2. It is clear that imposing low resistivity along the deeper oceanic crust induces significant lack of fit to the observed response. Thus, the inference of lack of interconnected conductive fluids along the deeper subduction interface from the model of Figure 2 appears valid and is a physical state compatible with the loss of S-wave low velocity coherence at similar depths.

### **S3.8 Test of Continuity of Near-Vertical Low Resistivity from Subduction Flux Melting Zone to Upper-Middle Arc Crust**

Continuous low resistivity is imaged below Mount Rainier in Figure 2 from nearly 100 km to only a few km depths. We test the possibility that the data are compatible with all low resistivity being separated into upper-middle crustal and upper mantle zones, with resistive middle and lower crust. The former then could potentially be assigned to non-arc sutured metasediments of the SWCC of Stanley et al. (1996) with all magmatic signatures being confined to the subcrust. We impose a 200 ohm-m tabular zone from ~10 - 44 km into the model of Figure 2 as outlined in Figure S8 and plot its forward response as pseudosections in Figure S10. This response has an nRMS misfit to the data of 3.78 compared to the preferred model with 1.78, so that it is rejected as a pos-

sibility. One sees in Figure S10 that significant misfit occurs in  $\rho_{yx}$  where values toward long period become too large relative to the data, plus corresponding misfit in  $\phi_{yx}$  where values for periods  $>100$  s are too small. Furthermore, starting from the a priori model of Figure S4 but with the 200 ohm-m zone fixed, a reinversion is done to see if an alternate model will fit the data adequately. The result is shown in Figure S11 yielding an nRMS of 2.20, also significantly greater than that for Figure 2. This inversion has attempted to recover a continuous structure toward the surface anyway by placing it trenchward of the imposed resistive block, so the need for continuous conductivity to fit the observations seems clear. Magmatic hydrothermal processes appear to persist to relatively high crustal levels, where they may or may not connect to earlier sediments.

## S4. EMSLAB Profile Analysis

### S4.1 Observed Data

The pseudosections showing the TM mode impedance functions and TE mode vertical field response emphasized in the 2D inversion are shown in Figure S12a-c over the period range of 0.008 to 6830 s, sampled at 41 logarithmically spaced points. With these older LP data, the longest average effective period is not as great as for CAFE. An x-axis (assumed strike) of N000E for all sites and all periods is again assumed, consistent with MT strikes presented later.

On this line, relatively high values of  $\rho_{yx}$  are seen over the first  $\sim 50$  km of the line on Siletzia rocks of the coastal range. This is helpful for resolving structure below at plate interface depths because it signifies that shallow screening sediments are largely absent. A bilobate low in  $\rho_{yx}$  is seen over the forearc Willamette Basin, where the modest central resistor results from local outcrop of Columbia River basalts [Wannamaker *et al.*, 1989]. Compact high  $\rho_{yx}$  values are seen below the relict Western Cascades plutonic rocks and, at shorter periods, low  $\rho_{yx}$  is seen denoting altered volcanics of the backarc Deschutes Basin.

The response in  $\phi_{yx}$  is again particularly diagnostic. One sees a subtle but distinct peak in  $\phi_{yx}$  appearing at the coastal-most site and extending inland across the forearc (Figure S12) at periods around 30 s. The peak in fact is strongest for the 4-5 sites at the coast, in contrast to CAFE. The peak weakens and moves to somewhat longer periods to a distance of  $\sim 60$  km inland, where it suddenly strengthens and begins at shorter periods. It grows to a maximum under the arc (Mount Jefferson), then moves to slightly longer periods in the backarc. There is no high phase anomaly extending from short periods to long under the arc such as was seen in CAFE.

An expected strong positive anomaly in  $\text{Re}(K_{zy})$  is seen again at the coastal sites at long periods, substantially stronger than for CAFE (Figure S12c). A paired negative-positive anomaly centered at 75 km denotes a maximum in depth of Willamette Basin sediments here. A stronger positive in  $\text{Re}(K_{zy})$  extends from 110 to 140 km and indicates the eastern flank of those sediments. Although it may be tempting to consider this positive and the negative immediately east as a pair, they really are caused by different structures. The negative in  $\text{Re}(K_{zy})$  is the result of termination of low resistivity altered volcanic rocks plus the conductive Cascades graben in this area. A fainter second negative in  $\text{Re}(K_{zy})$  at  $\sim 300$  s period represents the western edge of the Moho level conductor discussed with Figure 3 of the main text.

The nominal TE mode impedance quantities  $\rho_{xy}$  and  $\phi_{xy}$  are shown in the upper two panels of Figure S13a-c while the normalized vertical magnetic field reflecting along-strike changes in cross-strike current flow ( $\text{Re}(K_{zx})$ ) is in the lower panel (Figure S13c). We again see  $\rho_{xy}$  being of much lower amplitude near the coast than the TM  $\rho_{yx}$ , due largely to the flanking seawater and ma-

rine sediments. Numerous non-2D static shifts along the profile persisting to the longest periods are apparent in  $\rho_{xy}$  as well. Low phases at middle periods under the forearc reveal the basement to the Willamette Basin sediments. High  $\phi_{xy}$  under the Western Cascades in part may be just the decay of this anomaly toward long periods. Two narrow positive phase features extend to short periods from here, however, suggesting narrow fault zone structures. In the backarc, values of  $\rho_{xy}$  toward long periods tend to be higher than those of  $\rho_{yx}$ , which suggests this part of the profile lies on locally resistive basement with transition to conductive Great Basin crust and upper mantle to the south, as recognized by *Wannamaker et al.* [1989].

The vertical magnetic field quantity  $\text{Re}(K_{zx})$  in Figure S13c shows only a few features off-line violating a strict 2D assumption. Among these is a weak negative band at  $\sim 1000$  s period implying a small or distant gradient to higher conductivity to the north. Compact negative anomalies under the central forearc represent irregularities in the Willamette Basin with greater apparent thickness to the north in this area. A small positive anomaly at short periods below the Western Cascades is consistent with a small conductor to the south. There is a very mild negative in  $\text{Re}(K_{zx})$  values around 1000 s under most of the line implying a limited increase in profile-wide conductivity to the north.

#### S4.2 Geoelectric Trend Estimation

The histograms of principal axes of the impedance phase tensor for the EMSLAB line are plotted in Figure S14, again for nominal forearc and backarc areas by dividing the profile precisely in two, and for three period bands corresponding to sensitivity depth ranges from the upper middle crust to  $>200$  km. Apart from some deviation or indeterminacy in the short period band, the approximation of north-south strike in terms of impedance phase appears good. This seems compatible with  $K_z$  too, where the anomalies are seen predominantly in the zy component.

#### S4.3 Inversion Model Construction and Computed Model Responses

The 2D model is derived in a fashion analogous to CAFE. The forward mesh for Figure 3 of the main text is 335 x 71 nodes (including 10 air layers) extending to similar widths and depths. The starting and a priori model based on the integrated impedance again showed mildly low resistivities in the upper few km, and 100 ohm-m is used everywhere else. The inverted quantities again are the nominal TM mode  $\log_{10}(\rho_{yx})$  and  $\phi_{yx}$ , and  $\text{Re}(K_{zy})$  over the 41 periods. A handful of low TE mode  $\phi_{xy}$  values at middle short periods under the Willamette Basin were included to help focus the base of those sediments.

Total data set comprised  $\sim 3815$  data points, with an inversion of  $\sim 6420$  parameters, for the 2D distribution of  $\log_{10}(\rho)$ . Error floors of 3  $\log_{10}$  %, 2 deg, and 0.04 again were applied to apparent resistivity, phase and  $K_{zy}$  respectively, with one-half of those amplitudes applied to the long-period (LP) data. Starting nRMS for the EMSLAB data set was 13.2 while final nRMS misfit was 1.37 using similar inversion settings as for CAFE. The legacy seafloor sites were not included in this model [Evans et al., 2013] as they were not needed to resolve trench structure and their inclusion would make an unfair comparison with the other profiles.

The computed model response pseudosections for the primary data included in the inversion are plotted in Figure S12d-f for comparison to the data. Qualitatively the fit again is very good, replicating the main diagnostic features described previously. Note that the  $\phi_{yx}$  response peak of the conductive layer along the plate interface strengthens and moves to shorter periods at

the coast, in contrast to CAFE. This is the principal evidence for the high conductivity under the EMSLAB coastline and offshore toward the trench to shallow depths. There is still some tendency to have misfit right at the coast at the longest periods where the computed amplitude of  $\text{Re}(K_{zy})$  is somewhat greater than observed, for reasons unclear. However, this occurs to a much lesser extent than for CAFE.

The computed TE impedance responses for our inversion model are plotted in Figure S13d-f. Despite not explicitly including these data in the inversion, the model response and those data show qualitative agreement given the 2D limitations. There is a mild positive in  $\phi_{xy}$  near the coast at 50-100 s which represents the conductive trench structure offshore, although this anomaly is obscured somewhat by a probable 3D effect near  $y = 40$  km [Wannamaker, 1999]. The strong positive in  $\phi_{xy}$  under the Western Cascades in the 10-100 s range may be due as much to the decay of the influence of the resistive plutonic rocks on the TE response as to the mid-crustal conductor below. The low in  $\phi_{xy}$  under the Deschutes Basin area around 10 s is weaker in the computations than the data, consistent with our interpretation that the profile here lies on a resistive block with conductive Great Basin to the south.

#### S4.4 Test of Conductive Trench Structure

The inversion model of main text Figure 3 showed thick, high conductivity under the coast and shallow shelf. The implication of substantial subducted sediments and their role in reducing plate coupling is important, so we explore the range of permissible structure here. First we consider whether imposing a thin layer of resistive Siletz terrane rocks is compatible with the data (Figure S15a). The resulting inversion model (Figure S15b) fits the data just as well by concentrating the high trench area conductivity into a thinner layer just below the Siletz rocks. This model still does not show a conductive connection to the trace of the trench, so in Figure S15c we seed the starting model with such a connection while not imposing that it be preserved in the inversion. The model formed in Figure S15d is similar to that in S11b and the seed layer actually was reduced in conductance somewhat.

A similar outcome occurs when thicker Siletz rocks are imposed (Figure S15e-g) but the final fit to the data is worsened slightly (Figure S16). Although the resulting response is only subtly shifted to longer periods relative to the preferred inversion model, the best fit already is a bit shifted. Misfit for the four sites closest to the coast in the 10-300 s period range went from 2.18 to 2.42. Substantial conductivity occupying much of the shallow near-coast shelf seems inescapable. As a final proof of high conductance in this area, we replace most of the high conductance of the model of Figure S15g with a thin layer of 45 ohm-m and compute the response (Figure S15h). As Figure S16 shows, low conductance along the plate interface is incompatible with the measurements. Comparing CAFE and EMSLAB, there a correlation is seen between plate coupling and sub-shelf resistivity.

#### S4.5 Legacy Forward Model

For completeness, the original forward model of Wannamaker *et al.* [1989] is presented in Figure S17 in a color scheme compatible with other models of this paper. Its forward response is computed and compared to the data for the same frequencies and with the same error floors as used in the prior inversions, except the far eastern Earthscope site is not included. The resulting nRMS for the TM mode and  $\text{Re}(K_{zy})$  is 3.21. Although this certainly is not as close a fit as that of the pre-

ferred model of Figure 3 described above (1.37), it is a decent fit and the model explained many first-order features of the observations. The forward model showed a lower crustal fluid accumulation in the near forearc from slab eclogitization, although it did not represent the steady shallowing of those fluids across the crust as the arc is approached. Details of the forearc-backarc transition and lower crustal and upper mantle depths also are lacking. However, the model was sufficient to capture the deepening slab surface conductor below the Coast Range and make the inference that much released slab fluid rises through the crust before the arc is reached.

## **S5. Southwestern Oregon MT (SWORMT) Data Analysis**

The northeast trends below this profile including the main Siletz-Klamath terrane boundary, faults and folds within the southern Siletz terrane, and internal boundaries with the Klamath terrane, all are oblique to modern subduction trends and require a 3D inversion analysis. This is much more computationally intensive than the 2D inversion, however, and typically employs a more sparsely sampled (in period) data set and a more coarsely discretized model mesh than in 2D. Also, 3D inversion models exhibit very different sensitivity to different parts of the model volume, particularly when inverting profile data. For this reason, and for comparison to our other data sets along Cascadia, we focus our model assessment and interpretation on a cross-section through a 3D inverse model directly below the SWORMT profile.

### **S5.1 Observed Data**

Pseudosections showing the off-diagonal apparent resistivity and impedance phase data are shown in Figures S18 and S19. Although the SWORMT data are inherently 3D and thus do not align with a single coordinate system, we present the data in a trench-oriented coordinate system ( $x = N000$ ) to permit direct comparison with the nominal TM and TE mode pseudosections from the other profiles. The quasi-2D component of the tipper,  $\text{Re}(K_{zy})$  is also shown in Figure S18.  $K_{zx}$  data show the greatest departure from 2D behavior between 60 and 100 km along profile (Figure S19), reflecting the NE-trending Siletz-Klamath boundary, and around kms 125 and 175, collocated with internal boundaries and Cretaceous intrusions within the Klamath composite terrane.

There is a first-order influence by the conductive ocean, in accord with responses on our other profiles exemplified in the CAFE-MT starting model (Figures S4 and S5). This includes a region of low  $\varphi_{yx}$  and high  $\text{Re}(K_{zy})$  at 100-5000 s period, the onset of which moves to progressively longer period with increasing distance from the shore. Superimposed upon this coastal response is a region of high  $\rho_{yx}$  and low  $\varphi_{yx}$  at 1000-10000 s period that corresponds, in part, to the resistive Juan de Fuca slab. Reflecting enhanced north-south current flow within the flanking seawater and marine sediments,  $\rho_{xy}$  is of lower amplitude than  $\rho_{yx}$  at sites near the coast.

The response of  $\varphi_{yx}$  and  $\varphi_{xy}$  from 0-75 km along profile and around 10 s period is again diagnostic of resistivity structure along the plate interface. This region is characterized by moderately low impedance phase and, in contrast to the CAFE and EMSLAB profiles, does not exhibit the subtle phase high at 10-100 s period. As discussed in the main text, we consider this to be evidence for a sediment and fluid-starved plate interface along this portion of the subduction zone. There is a subtle ridge in  $\varphi_{yx}$  from 15-25 s period at distances of 50-90 km along the profile on land, but we will show that this represents a low-resistivity unit well within the upper plate. The onset of low  $\varphi_{xy}$  moves to progressively shorter periods moving inland from the coast, and is attributed to structure within the upper plate.

A pronounced peak in  $\phi_{yx}$  is however, observed starting at 75 km along profile, extending inland to the profile end. This phase peak moves to progressively longer periods with increasing distance along profile, is associated with high conductivity at and above the plate interface at depths of 30 km and greater (Figure 4), and is attributed to slab eclogitization.

Both  $\rho_{yx}$  and  $\rho_{xy}$  pseudosections show significant vertical striping primarily, but not exclusively, along the eastern half of the model section. These static shifts obscure much of the upper-plate structure, but phase and tipper sections reveal significant lateral variability in subsurface resistivity within the Klamath composite terranes. A prominent reversal in  $K_{zy}$  at 130 km along profile is accompanied by strong variations in the phases, which are sometimes out of normal quadrants. These strong variations are attributed in part to a series of large Cretaceous plutons (e.g. Grants Pass, Grayback, and Ashland plutons) intruded into the older Klamath composite terranes. 3D behavior is evident in non-zero  $K_{zx}$  in the vicinity of these plutons as well an extensive region of negative  $K_{zx}$  at short to intermediate period near the Siletz-Klamath boundary.

## S5.2 Inversion Model Construction and Computed Model Responses

The measured data were inverted in 3D using the MPI-parallelized ModEM code of Kelbert et al (2014). The inversion was carried out on a finite-difference model mesh of 98 x 98 x 50 cells aligned with geographic north (480,200 model parameters). A uniform horizontal cell size of 4 x 4 km was employed over a 320 x 320 km region incorporating and surrounding the area where MT stations are present. Outside of this region, horizontal cell size increases geometrically with the total mesh measuring more than 1200 x 1200 km in the north and east directions. Model cell thicknesses increase geometrically with depth from an initial value of 75 m; total model depth exceeds 500 km to ensure that calculated anomalous electric-fields vanish at the base of the model. Bathymetry and coastline geometry of the Pacific Ocean were included a priori in an otherwise homogeneous 100  $\Omega$ -m starting model, with seawater resistivity fixed at 0.333 ohm-m.

A three-step inversion procedure was carried out. Initially, a 3D inversion of complex impedance and tipper data was performed using 17 periods ranging from 1–10000 seconds. Impedance data errors were used subject to an error floor (ceiling) of 5% (15%) of  $|Z_{ij}|$  while the tipper data error floor was 0.01. The total data set comprised 7650 complex data points. The initial inversion completed 132 iterations in 7 days with a reduction in nRMS data misfit from 3.27 for the starting model to 1.67; nRMS misfit values are calculated using the applied errors.

A second inversion of off-diagonal resistivity and phase, together with tipper data, was started using the output of the initial inversion as the starting model. This inversion was carried out to improve fit to the measured impedance phase data, and particularly to focus on the subtle ridge in  $\phi_{yx}$  described above, and to reduce the effects of static shifts in the measured data (Figures S18 and S19) on the inversion. To achieve this, 1° errors were imposed on phase data and a relatively large 10% relative error was applied to the apparent resistivity data; tipper errors were unchanged. This second inversion completed 27 iterations in just over 2 days. Overall nRMS increased to 2.40 reflecting compromise in fit elsewhere in the model by focusing upon the phase data. A final 3D inversion was carried out using data and errors identical to the initial inversion, but with the output model from the second inversion as the starting model. This inversion completed 46 iterations in 4 days with a final nRMS misfit of 1.67.

The response of the final inverse model is shown as pseudosections in Figures S18 and S19 for the off-diagonal apparent resistivity and phase values as well as the real component of the tipper. Qualitatively the fit is quite good, with measured responses replicating the features discussed

previously. Exceptions include  $\phi_{yx}$  at 500-5000 s period and from 75-125 km, where the synthetic phase response somewhat underfits the measured phase data. Also, measured  $\phi_{xy}$  below 1000 s period can approach or exceed  $90^\circ$ , values that are not recovered in the computed response. The real component of the impedance is very small in this case, and may be underfit relative to the error floor. Others have shown that they sometimes can be simulated by the interaction of large-scale structure with small heterogeneity closer to the MT stations [e.g., *Ichihara and Mogi, 2009*]. Possibly they could be accommodated through a combination of a finer mesh (prohibitive at present computationally) and iterative static distortion removal during inversion [e.g., *Avdeeva et al., 2014*]. They have been observed occasionally in  $\phi_{xy}$  on the other profiles as well.

A breakdown of the nRMS by data component, site, and period is shown in Figure S20. A clear reduction in misfit between the starting and final inverse models can be seen for all components and the final nRMS misfit is observed to be distributed evenly among the different components, with the largest residuals corresponding to the diagonal impedance elements. The marked reduction in the diagonal apparent resistivity and phase values is due to the predominantly 2D starting model, the impedance response of which is close to zero for the diagonal elements.

The distribution of nRMS by site, shown only for the 45 sites located along the SWORMT profile, is again relatively uniform, with a region between sites 31-39 exhibiting elevated nRMS misfit, particularly in the impedance phase and tipper components. The elevated phase and tipper misfit is attributed to static shifts in the apparent resistivity data which the inversion has fit at the expense of the tipper and phase data. The distribution of nRMS misfit versus period is relatively uniform, but shows some increase, particularly in impedance phase and tipper, at the shortest periods. This is not unexpected, as the horizontal cell size (4 km) is comparable or larger than the skin depth at the shortest periods considered in the inversion.

### S5.3 Test of Subduction Conductance under Coast

The inversion model in Figure 4 is relatively resistive above the slab beneath the shallow shelf and extending on land to km 70 along profile. The implied absence of substantial subducted sediments is important, so we consider whether imposing a thin layer of conductive sediments is compatible with the data, comparable to the CAFE-MT line (Figure S21). Starting from the original model, we added a conductive channel at the plate interface from the trench to  $\sim 25$  km slab depth. Along strike the channel was allowed to run for 200 km.

The forward response of such a modified model is shown in Figure S22 for two stations 10 and 75 km along the profile. The primary test for permissibility of this high conductivity zone lies in the  $\phi_{yx}$  response in the 10-100 s period ranges, similar to our other profiles. At the western station, the addition of a 12 or 25 ohm-m conductive layer produces a distinct peak in  $\phi_{yx}$  between 20 and 500 s period that is not present in the measured data. This observation holds true at nearly all sites within 30 km of the coast. We thus conclude that high conductance along the plate interface near the coast is inconsistent with the measured data.

At the eastern station, a subtle phase peak at  $\sim 25$  s is seen, as pointed out previously when discussing the observed pseudosections. This has been fit qualitatively by the inversion model of Figure 4 through appearance of the deep upper-plate conductor (DUC) in the 10-20 km depth range. The addition of a conductive layer again produces a much stronger peak in  $\phi_{yx}$ , but it occurs at longer periods than that of the DUC structure. Thus, a plate interface conductor appears unlikely at these distances along the profile from the coast as well.

## S6. Klamath-Modoc Profile Analysis

### S6.1 Observed Data

The pseudosections showing the TM mode impedance functions and TE mode vertical field response emphasized in the 2D inversion of this profile are shown in Figure S23 over the period range of 0.005 to 17480 s, sampled at 45 logarithmically spaced points. Signal strength generally was good for this campaign so the total period range is somewhat greater. An x-axis (assumed strike) of N000E for all sites and all periods is again assumed, in part for consistency with the other profiles. We will examine dependence of model features on assumed strike.

The character of MT responses on this profile differs somewhat from the other two lines. We do see again quite low  $\phi_{yx}$  as much as 200 km inland from the coast which reveals presence of the Gorda plate and influence of the seawater, and there are low  $\rho_{yx}$  and high  $\phi_{yx}$  at shorter periods east of the arc (Lassen Peak) showing presence of shallow altered volcanic beds. There also is the usual peak at long periods in  $\text{Re}(K_{zy})$  near the coast reflecting the marine transition (Figure S23c). However, we do not see anywhere along the forearc a continuous albeit subtle peak in  $\phi_{yx}$  as evidence of a conductive plate interface or exsolution and upward migration of fluids therefrom such as on the previous profiles. Instead there are compact highs in  $\phi_{yx}$ , especially  $\sim 80$  km inland in the 0.1-10 s range and 150-180 km inland in the 1-500 s range. This lack was interpreted in the main text to be the result of unusually shallow plate dip inland for a distance of  $\sim 150$  km [McCrory *et al.*, 2012] so that there is no mantle wedge in this interval. A weaker ridge in  $\phi_{yx}$  occurs east of the arc around 200 s indicating low resistivity at Moho and subcrustal depths. A compact negative in  $\text{Re}(K_{zy})$  in the 0.1-10 s range just west of Lassen Peak corresponds to the western edge of the conductive near-surface volcanics. High  $\rho_{yx}$  is seen below and just east of the Sacramento River probably reflecting eastern Klamath plutons [Allen and Barnes, 2006].

Similar to before, the nominal TE mode impedance quantities  $\rho_{xy}$  and  $\phi_{xy}$  are shown in Figure S24a-b while the normalized vertical magnetic field reflecting along-strike changes in cross-strike current flow ( $\text{Re}(K_{zx})$ ) is in the lower panel (Figure S24c). There are the expected lower values of  $\rho_{xy}$  and higher  $\phi_{xy}$  near the coast compared to the TM. Numerous non-2D static shifts along the profile persisting to the longest periods are seen again in  $\rho_{xy}$ . Two very prominent narrow lows in  $\rho_{xy}$  reside just west of the Sacramento River and have associated narrow highs in  $\phi_{xy}$ . These hence must be local 3D effects, perhaps associated with intense alteration and numerous historic mine workings of the Mad Mule Mountain area. Similar to the TM mode, low  $\rho_{xy}$  and high  $\phi_{xy}$  at shorter periods east of the arc show presence of the altered volcanic blanket. There at the longer periods ( $\sim 200$  s), a band of high  $\phi_{xy}$  values is seen similar to the TM mode but with short wavelength lateral variations not expected in purely 2D TE behaviour. At the longest periods, there are some intense local anomalies in  $\phi_{xy}$  that do not seem to be statistical noise but again are believed to be local 3D effect which, in our experience in the western U.S., appear more associated with the weaker (in response amplitude) nominal TE mode.

A few anomalies in  $\text{Re}(K_{zx})$  also display non-ideal dimensionality (Figure S24c). A compact high around 100 s and 120 km inland has a stronger correspondent in  $\text{Re}(K_{zy})$  suggesting that strike deviates from N000 here. Intense compact anomalies are associated with the Mad Mule Mtn district again. A local negative in  $\text{Re}(K_{zx})$  occurs around 10 s period as the line crosses Eagle Lake. Finally, there is a weak, broad anomaly in  $\text{Re}(K_{zx})$  in the backarc in the 300-3000 s range indicative of large-scale gradient in conductivity from south to north.

## S6.2 Geoelectric Trend Estimation

The histograms of principal axes of the impedance phase tensor for the Klamath-Modoc line are plotted in Figure S25 again for a nominal forearc and a backarc area by dividing the profile in two, and for the three period bands. In the short period band, the forearc area suggests a geoelectric strike a bit east of north, while the back appears bimodal with north-south and northwest-southeast groupings. This may reflect families of oblique strike-slip and north-south normal faulting in the southern Modoc Plateau [Blakely *et al.*, 1997]. At longer periods, the axes appear to be consistently northnorthwest-southsoutheast to northwest-southeast. This is similar to the experience of *Park and Ostos* [2013] who identified a principal axis of N025W in their data. It presents a quandary for choosing the best strike for 2D inversion. On the one hand, a NNW-SSE strike initially appears appropriate at face value. However, as discussed by *Torres-Verdin and Bostick* [1992], it is TM mode quantities defined with the electric field direction along the trend of the profile which possess zero-mean anomalies and our profile is nearly east-west. Thus we construct inversion models using both a N000 and N025W strike assumption and compare principal features. First we examine the N000 results.

## S6.3 Inversion Model Construction and Computed Model Responses

The 2D model mesh for Figure 5 of the main text is 553 x 71 nodes (including 10 air layers) extending to similar widths and depths as the other profiles. The starting and a priori model based on the integrated impedance again have mildly low resistivities in the upper few km, and 100 ohm-m is used everywhere else. The inverted quantities once more are the nominal TM mode  $\log_{10}(\rho_{yx})$  and  $\phi_{yx}$ , and  $\text{Re}(K_{zy})$  over the 45 periods. The data set comprised ~9215 data points, with an inversion of 10205 parameters, for the 2D distribution of  $\log_{10}(\rho)$ . Error floors of 3  $\log_{10}$  %, 2 deg, and 0.04 again were applied to apparent resistivity, phase and  $K_{zy}$  respectively, with one-half of those amplitudes applied to the LP data. Starting normalized root-mean-square (nRMS) for the Klamath-Modoc data set was 16.3 while final nRMS misfit was 1.47 using similar inversion settings as for CAFE. This is a larger model requiring ~8 hours of run-time on the desktop PC.

The computed model response pseudosections for the primary data included in the inversion and a N000 strike assumption are plotted in Figure S23d-f for comparison to the data, showing a qualitatively good fit again. The compact high  $\phi_{yx}$  80 km inland in the 0.1 – 10 s range, and the high  $\text{Re}(K_{zy})$  in from 80-130 km inland from 10-100 s, correspond to the underthrust Franciscan melange metasediments below South Mountain area in main text Figure 5. The strong high in  $\phi_{yx}$  from 1-100 s period below the Sacramento River area is evidence for the compact eclogitization conductor where the plate suddenly deepens. Its response in  $\text{Re}(K_{zy})$ , however, appears to be masked by flanking features; it may be responsible for subduing the eastern limit of the Franciscan response. Subtle interruptions of the low  $\phi_{yx}$  band below Lassen Peak and Snowstorm-Shinn Mountains are the evidence for the modest but through-going conductors connecting upper and lower crust there (Figure 5). This time, the fit to  $\text{Re}(K_{zy})$  right at the coast at the longest periods appears good.

The compute TE responses are in Figure S24d-f and show qualitative agreement in places, but the usual problems in other places. There are again numerous statics in the data not reproduced in the computed  $\rho_{xy}$ , and the 3D effects around Mad Mule Mtn are absent in the calculations. Under the backarc area between Lassen Peak and Snowstorm Mtn, the observed values stay low in a broad wavelength fashion to long periods. This could be explained by finite north-south strike of

the conductive upper crustal volcanic blanket, which thins toward the Sierra Nevada, which would be consistent with the mild negative in  $\text{Re}(K_{zx})$  in the 300-3000 s period range. This possibility concerns us that inclusion of TE mode data by *Park and Ostos* [2013], even though downweighted, may have lead to the inference of higher conductivity below the arc and backarc than is fully warranted.

One of the most striking differences between the observed and computed TE results is under the Sacramento River area. There, very little in the way of an observed TE anomaly (e.g., high  $\phi_{xy}$ ) exists that might have corresponded to the high  $\phi_{yx}$  used to infer the eclogitization. The computed TE results on the other hand show a very large positive  $\phi_{xy}$  anomaly (Figure S24e) at slightly shorter periods. However, this anomaly is entirely due to the decay in the response of the highly resistive, interpreted plutonic volumes overhead under and east of the Sacramento River. In reality, these resistors may have significantly finite strike extent so that they reach a static limit in the TE mode and so  $\rho_{xy}$  does not decay toward longer periods. Thus, the observed TE results are consistent with our interpretation in light of plausible 3D effects more prevalent in that mode.

#### **S6.4 Alternate Model with X = N025W**

The WB and LP data of the Klamath-Modoc profile were rotated 25 degrees CCW and remerged to test effect of rotation angle. This is the strike used by *Park and Ostos* [2013]. The resultant observed pseudosections are in Figures S26 and S27. The basic features underlying the principal structures have not changes significantly. This new rotation angle appears less appropriate for the vertical magnetic field right near the coast because now there is a greater proportion lying in  $\text{Re}(K_{zx})$ . On the other hand, the anomaly 80 km inland associated with underthrust Franciscan is slightly stronger in  $\text{Re}(K_{zy})$  and weaker in  $\text{Re}(K_{zx})$ . Otherwise, small and large scale static and other off-line structures appear to be acting similarly.

The resulting 2D inversion model is shown in Figure S28. Data fits are similarly good to those of the N000 results and we have plotted the computed pseudosections with the observations. All principal structural features of Figure 5 of the main text appear also in Figure S28; if anything, the structural contrasts in the latter figure are slightly greater. In particular, the interpreted upper mantle flux melting zone below Lassen Peak is of somewhat lesser resistivity, centered in the 50-100 km depth range. The underplating zone beneath Snowstorm Mtn area is more pronounced and that under Lassen Peak itself somewhat more visible. The strong, compact conductor associated with eclogitization under the Sacramento River area is similar for this orientation. We conclude that the resistivity cross section and inferences from it are robust to modest changes in assumed strike.

#### **S6.5 Test of Subduction Conductance under Coast**

The inversion models of main text Figure 5 and S28 show high resistivity at plate interface depths under the coast and seaward with implications for plate coupling and possible structural disruption. To test the high resistivity requirement, two models are considered (Figure S29). One has a thin layer of moderate resistivity (35 ohm-m) extending as far inland as South Mountain. The other has a thin layer of lower resistivity (7 ohm-m) but only extending to under the Eel River basin. Calculations are in Figure S30 and clearly show that these test models are not compatible with the data. For the long layer for example, using the westernmost 10 sites, the local nRMS increases from 1.18 to 3.47. The only difference in the two tests is that the misfit for the shorter layer does

not, understandably, persist as far as South Mountain. The exceedingly high resistivities existing under the coastal area to depths much shallower than the plate interface appears required by the data and is compatible with the seismicity shown in Figure 5. A shallow view of structure under the delta region is shown in Figure 6 with a diagnostic MT sounding plotted in Figure S31.

## S7. ABCS Profile Analysis

### S7.1 Observed Data

The pseudosections of both nominal TM and TE impedance functions and both tipper elements (real components) are plotted in Figure S32a-c and g-i. As LP data only, they extend over the period range 4.3 through 10240 s, which is roughly the lower half of the period range of the U.S. MT profiles. An x-axis of N330 (N30W) is used for direct comparison to the results of *Soyer and Unsworth* [2006], who estimated this as average geoelectric strike based also on phase tensor analysis, and none additional is carried out.

High values of  $\rho_{yx}$  are seen over the first ~50 km of the line on Wrangellia terrane rocks of southern Vancouver Island. Two lows in  $\rho_{yx}$  appear flanking Georgia Strait where metasediments accreted between the island and the mainland are believed to lie. Farther east across the Coastal Belt,  $\rho_{yx}$  is moderately high, tempered somewhat perhaps by low-resistivity sediments of the Fraser River delta. Higher values again are seen east of the Garibaldi-Baker (G/B) volcanic arc axis, especially across the Fraser fault zone, punctuated by a few single-site lows denoting local conductive heterogeneity. This is especially the case toward the eastern Omineca belt. Generally,  $\rho_{yx}$  decreases from shorter periods toward the longer.

A peak in  $\phi_{yx}$  appears at the first coastal site and extends inland, albeit unevenly, across Vancouver Island (Figure S32b) at periods around 30 s. High phase extends to the longest periods at the sixth site in, which is not characteristic 2D behaviour and is considered a local 3D effect. Just east of Georgia Strait at the ninth site, a quasi-horizontal peak in  $\phi_{yx}$  is seen extending and amplifying toward G/B. This peak reveals the presence of a Moho level conductor as seen in the model of Figure 7 of the main text believed to represent released slab fluids accumulating near Moho levels. At the Fraser fault zone just east of G/B, a pronounced increase in  $\phi_{yx}$  is observed in the 10-50 s period range persisting to the far east end of the profile. It is especially strong at the easternmost four sites and is diagnostic of increasing conductivity with depth from the middle toward the lower crust in this backarc domain. For  $T > 300$  s as one crosses from the volcanic forearc to the backarc, a sudden increase in overall values of  $\phi_{yx}$  is seen which marks the transition from the resistive Juan de Fuca plate to less resistive backarc upper mantle.

Similar to CAFE, high  $\text{Re}(K_{zy})$  is seen near the coastline due to the seawater and marine sediments to the west, which tapers and moves to longer periods inland (Figure S32c). Strongly negative values at ~200 s and less exist for the three sites on the western side of Georgia Strait, with modestly positive values to the east of the strait. Forward model tests indicate that strait bathymetry would produce such strong responses only for the single sites on each side of the strait for  $T < 50$  s, so additional conductive structure in the crust must exist in this vicinity. A few site-to-site anomalies short periods (10-20 s range) east of G/B reflect small inhomogeneity not of direct interest here. A negative anomaly in  $\text{Re}(K_{zy})$  of modest amplitude but large spatial scale in the 30-1000 s range near the east end of the profile indicates a large conductor just farther east, presumably under the Omineca terrane.

The nominal TE mode impedance quantities  $\rho_{xy}$  and  $\phi_{xy}$  are shown in the panels of Figure

S32g-h while the normalized vertical magnetic field reflecting along-strike changes in cross-strike current flow ( $\text{Re}(K_{zx})$ ) is in the bottom left panel (Figure S32i). As occurs often,  $\rho_{xy}$  exhibits near-vertical streaking on the pseudosection revealing local structures of finite strike that do not obey the physics of 2D TE responses. Such local distortions extend to  $\phi_{xy}$  at three sites also, two near the Fraser fault zone and one to the east as the Omineca belt is approached. However, under those three complications one can observe a quasi-horizontal peak in  $\phi_{xy}$  from the Fraser fault to the Omineca belt showing existence of a conductive lower crustal layer as did  $\phi_{yx}$ .

The vertical magnetic field quantity  $K_{zx}$  in Figure S32i shows that this profile has several structures offline violating the strict 2D assumption worth discussing. Positive  $\text{Re}(K_{zx})$  in the 30-300 s range under much of Vancouver Island indicates increased conductivity to the south, and a likely candidate would be the thickening Tertiary accreted section such as makes up the Olympic Mountains. Strong positive values exist at the west side of Georgia Strait, though not as high as those of  $\text{Re}(K_{zy})$ , implying that possible Mesozoic accretionary sediments there may strike more northwesterly than N30W. This continues in a subdued fashion to the complementary negative anomaly on the other side of the strait. For periods of  $\sim 30$  s and less across the Coastal Belt, positive  $\text{Re}(K_{zx})$  can be explained by a greater quantity of conductive Fraser River delta sediments to the south of the profile compared to the north. The anomaly flips sign for a short distance as the Fraser fault zone is crossed implying higher shallow conductivity now sits to the north.  $\text{Re}(K_{zx})$  is essentially featureless across the rest of the Intermontane and Omineca belts.

## S7.2 Model Construction and Computed Model Responses

As with the other profiles, the 2D inversion of the ABCS profile utilizes the TM mode apparent resistivity and impedance phase, and  $\text{Re}(K_{zy})$ , as these are more robust for the 2D assumption than the TE impedance quantities. Additionally, we found  $\phi_{yx}$  at the second site from the coast to be highly sensitive to rotation and thus invert only its  $\rho_{yx}$ . With the local 3D effect suspected at the sixth site in, only periods  $\leq 200$  s for this site were included in the inversion. To ease discretization requirements, we did not invert  $\text{Re}(K_{zy})$  for periods  $< 10$  s.

The forward mesh for Figure 7 of the main text is 325 x 71 nodes (including 10 air layers) extending to similar widths and depths as for CAFE and using the same a priori resistivity structure. The inverted quantities are the nominal TM mode  $\log_{10}(\rho_{yx})$  and  $\phi_{yx}$ , and  $\text{Re}(K_{zy})$  over the 28 periods from 4.3 to 10240 s. Error floors of 3  $\log_{10}$  %, 2 deg, and 0.06 were applied to apparent resistivity, phase and  $\text{Re}(K_{zy})$  respectively. Somewhat higher floors for  $\text{Re}(K_{zy})$  were used compared to the other profiles due to the greater presence of  $K_{zx}$ . Starting normalized root-mean-square (nRMS) for the ABCS data set was 17.8 while final nRMS misfit was 2.34. Decreasing the regularization factor did not improve final fit nor bring out additional structure significantly.

The computed model response pseudosections for the primary data included in the inversion are plotted in Figure S32d-f for comparison to the data. Qualitatively the fit is good, reproducing the main diagnostic features discussed above. Note the local disagreement in  $\phi_{yx}$  at the second and sixth site from the coast which were omitted due to suspected local 3D behavior. Nevertheless, the high  $\rho_{yx}$  values at sites 2-4 from the coast on Vancouver Island appear to compel the appearance of a high resistivity pinchout below them in Figure 7 at depths near the plate interface model of *McCroly et al.* [2012]. The anomaly in  $\text{Re}(K_{zy})$  across Georgia Strait and presumed accreted sediments is not quite as strong and is more symmetric than observed, but is qualitatively fit and sufficient to demonstrate that Georgia Strait seawater is not sufficient to explain the response. Other features in the primary inverted data are fit well.

The computed TE impedance responses for our inversion model are plotted in Figure S32j-k. The observed and computed TE apparent resistivities show obvious differences due to the several static and other local structural features in the former. That is similarly the case for the three sites showing strong local 3D effects in  $\varphi_{xy}$  as well. However, most of the rest of the pseudosection in  $\varphi_{xy}$  resembles the data to first order. There is a mild positive in  $\varphi_{xy}$  near the coast at 50-100 s which represents the conductive trench structure offshore, plus the quasi-tabular high in  $\varphi_{xy}$  under the Intermontane and Omineca belts representing conductive lower crust.

Given the relatively small number of sites on Vancouver Island, we cannot present a detailed picture of structure below that area. Thus we make no explicit sensitivity tests as done for the other profiles. Effectively, the westernmost site in the ABCS profile is 40 km farther from the trench than is the corresponding site on the CAFE MT line so an assessment of plate coupling by resistivity is not possible. However, apart from accreted material under the Georgia Strait area, the overall estimated depth to increased conductivity in the lower crust under Vancouver Island is near the subducting plate interface and not at a significantly higher level in the crust such as the conjectured E layer [Ramachandran *et al.*, 2006]. Resistivity structure east of the strait is considered well resolved.

## Disclaimer

Any use of trade, product, or firm names is for descriptive purposes only and does not imply endorsement by the U.S. Government.

## Supporting References

- Avdeeva, A., M. Moorkamp, D. Avdeev, M. Jegen, and M. Meinsopust (2014), Three-dimensional inversion of magnetotelluric impedance tensor data and full distortion matrix, *Geophys. J. Int.*, in press.
- Blakely, R. J., R. L. Christiansen, M. Guffanti, R. E. Wells, J. M. Donnelly-Nolan, L. J. P. Muffler, M. A. Clynne, and J. G. Smith (1997), Gravity anomalies, Quaternary vents, and Quaternary faults in the southern Cascade Range, Oregon and California: implications for arc and backarc evolution, *J. Geophys. Res.*, 102, 22,513-22,527.
- Booker, J. R. (2013), The magnetotelluric phase tensor: a critical review, *Surv. Geophys.*, DOI 10.1007/s10712-013-9234-2.
- Booker, J. R., A. Favetto, and M. C. Pomposiello (2004), Low electrical resistivity associated with plunging of the Nazca flat slab beneath Argentina, *Nature*, 429, 399-404.
- Caldwell, T. G., H. M. Bibby, and C. Brown (2004), The magnetotelluric phase tensor, *Geophys. J. Int.*, 158, 457-469.
- Chave, A. D., and A. G. Jones, eds (2012), *The Magnetotelluric Method: Theory and Practice*, Cambridge University Press, 552 pp.
- Chen, J., H. W. Dosso, and M. Ingham (1993), Electromagnetic induction in the New Zealand South Island, *Phys. Earth Planet. Int.*, 81, 253-260.
- deGroot-Hedlin, C. M., and S. C. Constable (1990), Occam's inversion to generate smooth, two-dimensional models from magnetotelluric data, *Geophysics*, 55, 1613-1624.
- DeLugao, P. P., and P. E. Wannamaker (1996), Calculating the two-dimensional magnetotelluric Jacobian in finite elements using reciprocity, *Geophys. J. Int.*, 127, 806-810.
- Dosso, H. W., J. Chen, and C. J. Bromley (1996), EM induction in the New Zealand Southern

- Alps region, *J. Geomag. Geoelec.*, 48, 247-255.
- Egbert, G. D. (1997), Robust multiple-station magnetotelluric data processing, *Geophys. J. Int.*, 130, 475-496.
- Ghosh, A., J. E. Vidale, J. R. Sweet, K. C. Creager, A. G. Wech, and E. E. Brodsky (2010), Rapid, continuous streaking of tremor in Cascadia, *Geochemistry, Geophysics, Geosystems*, 11, Q12010, 10 pp.
- Hohmann, G. W., and A. P. Raiche (1988), Inversion of controlled source electromagnetic data, *in* *Electromagnetic methods in applied geophysics*, edited by M. N. Nabighian, 1, Soc. Explor. Geophys., Tulsa, OK, 443-468.
- Ichihara, H., and T. Mogi (2009), A realistic 3-D resistivity model explaining anomalous high magnetotelluric phases: the L-shaped conductor model, *Geophys. J. Int.*, 179, 14-17.
- Kelbert, A., N. Meqbel, G. D. Egbert, and K. Tandon (2014) ModEM: a modular system for inversion of electromagnetic geophysical data, *Computers and Geosciences*, 66, 40-53.
- Ledo, J. (2005), 2-D versus 3-D magnetotelluric data interpretation, *Surv. Geophys.*, 26, 511-543.
- Mackie, R. L., L. Bennett, and T. R. Madden (1988), Long period magnetotelluric measurements near the central California coast: a land-locked view of the conductivity structure under the Pacific Ocean, *Geophys. J. Int.*, 95, 181-194.
- Simpson, F., and K. Bahr (2005), *Practical magnetotellurics*, Cambridge Univ. Press, 254 pp.
- Siripunvaraporn, W., G. Egbert, and M. Uyeshima (2005), Interpretation of two-dimensional magnetotelluric profile data with three-dimensional inversion: synthetic examples, *Geophys. J. Int.*, doi: 10.1111/j.1365-246X.2005.02527.x.
- Tarantola, A. (1987), *Inverse Problem Theory*: Elsevier, New York, 613 pp.
- Torres-Verdin, C., and F. X. Bostick, Jr. (1992), Principles of spatial surface electric field filtering in magnetotellurics: electromagnetic array profiling (EMAP), *Geophysics*, 57, 603-622.
- Vozoff, K. (1991), The magnetotelluric method, *in* *Electromagnetic methods in applied geophysics*, edited by M. N. Nabighian, 2B, Soc. Explor. Geophys., Tulsa, 641-711.
- Wannamaker, P. E. (2005), Anisotropy versus heterogeneity in continental solid earth electromagnetic studies: fundamental response characteristics and implications for physico-chemical state, *Surv. Geophys.*, 26, 733-765.
- Wannamaker, P. E. (1999), Affordable magnetotellurics: interpretation in natural environments, *in* *Three-dimensional electromagnetics*, edited by Oristaglio, M., and B. Spies, Geophys. Develop. Ser., 7, Soc. Explor. Geophys., Tulsa, 349-374.
- Wannamaker, P. E., J. A. Stodt, and L. Rijo (1987), A stable finite element solution for two-dimensional magnetotelluric modeling, *Geophys. J. Roy. Astron. Soc.*, 88, 277-296.
- Wannamaker, P. E., G. R. Jiracek, J. A. Stodt, T. G. Caldwell, V. M. Gonzalez, J. D. McKnight, and Porter, A. D. (2002), Fluid generation and pathways beneath an active compressional orogen, the New Zealand Southern Alps, inferred from magnetotelluric data, *J. Geophys. Res.*, 107, ETG 6, 1-22.
- Young, C. T., J. R. Booker, R. Fernandez, G. R. Jiracek, M. Martinez, J. C. Rogers, J. A. Stodt, H. S. Waff, and P. E. Wannamaker (1988), Verification of five magnetotelluric systems in the mini-EMSLAB experiment, *Geophysics*, 53, 553-557.
- Zhdanov, M. S. (2002), *Geophysical inverse theory and regularization problems*: Elsevier, Oxford, 609 pp.

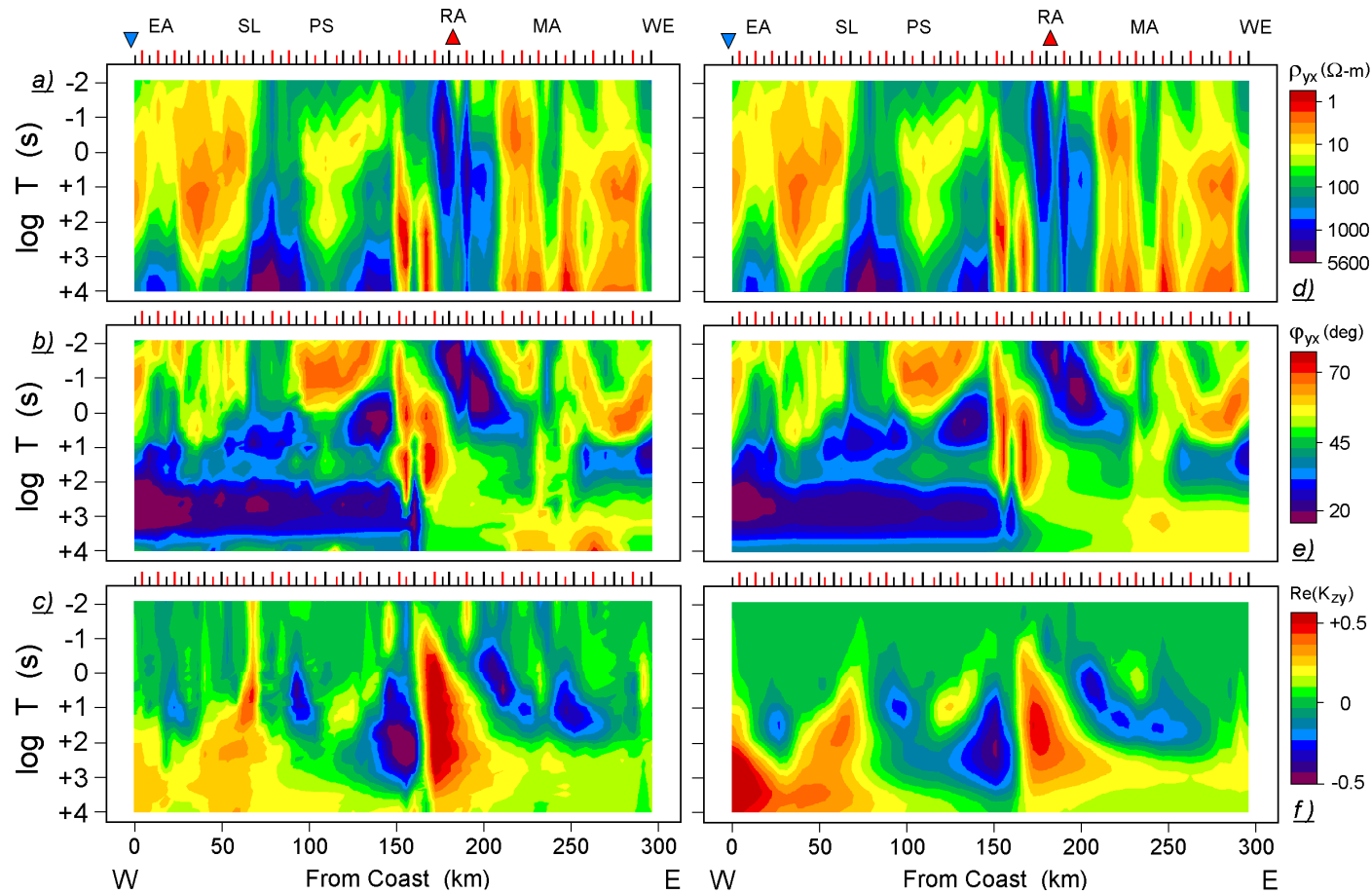


Figure S1. Left: Pseudosections of primary observed nominal MT quantities along the CAFE transect: (a), TM mode apparent resistivity  $\rho_{yx}$ ; (b), TM mode impedance phase  $\phi_{yx}$ ; (c), real component of TE mode normalized vertical magnetic field  $\text{Re}(K_{zy})$ . Units are logarithmically spaced ohm-m, linear degrees, and dimensionless. These observations are emphasized in the 2D inversion models. Right: Pseudosections of primary computed MT quantities along the CAFE transect from the model of main text Figure 2. Red ticks show locations where LP recordings were made as well as WB. Physiographic locations as in main text.

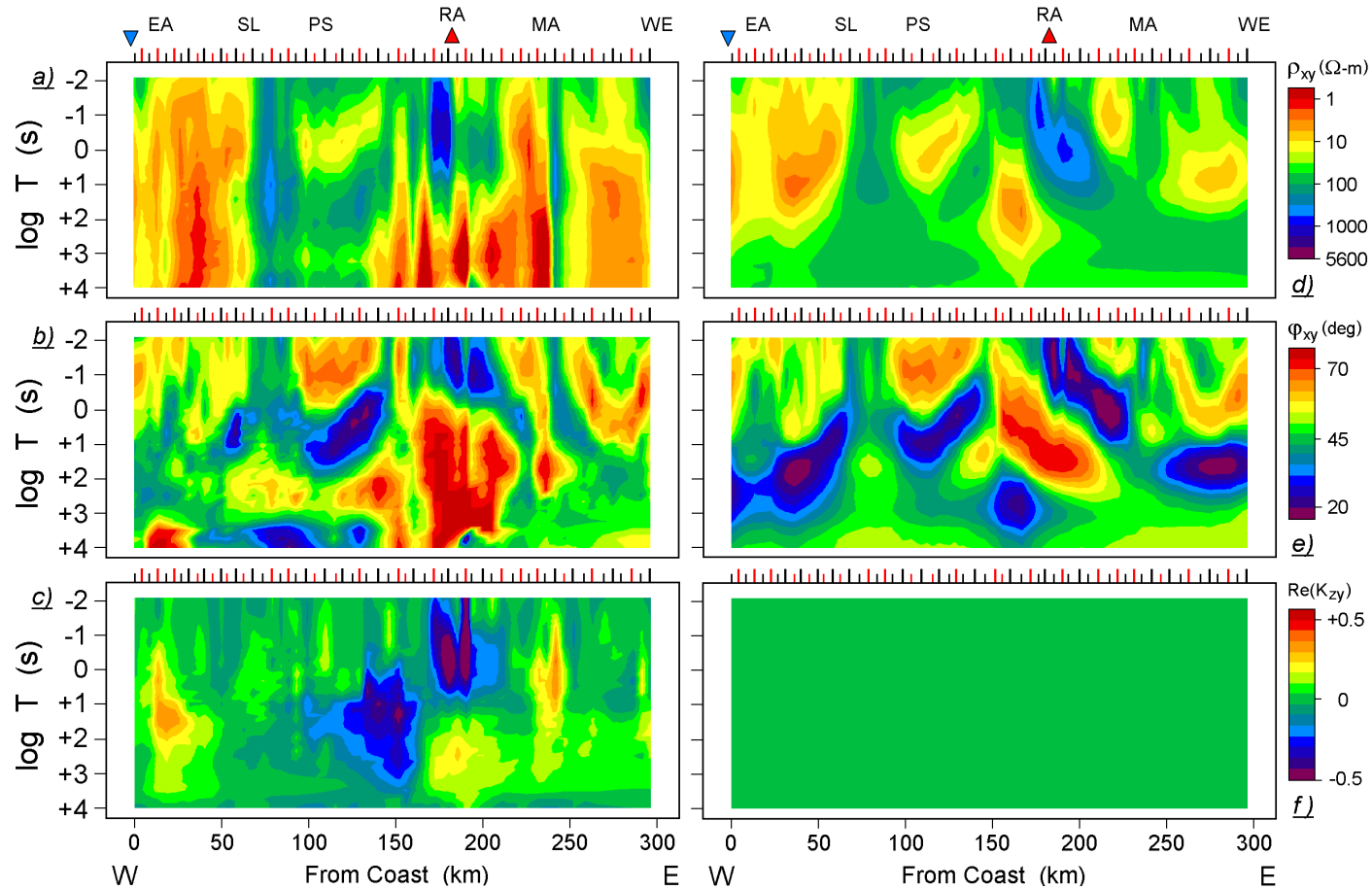


Figure S2. Left: Pseudosections of secondary observed MT quantities along the CAFE transect: (a), TE mode apparent resistivity  $\rho_{xy}$ ; (b), TE mode impedance phase  $\phi_{xy}$ ; (c), real component of TM mode normalized vertical magnetic field  $\text{Re}(K_{zy})$ . Units are logarithmically spaced ohm-m, linear degrees, and dimensionless. These observations are de-emphasized in the 2D inversion models. Right: Pseudosections of secondary computed MT quantities along the CAFE transect from the model of main text Figure 2.  $\text{Re}(K_{zy})$  is zero in 2D.

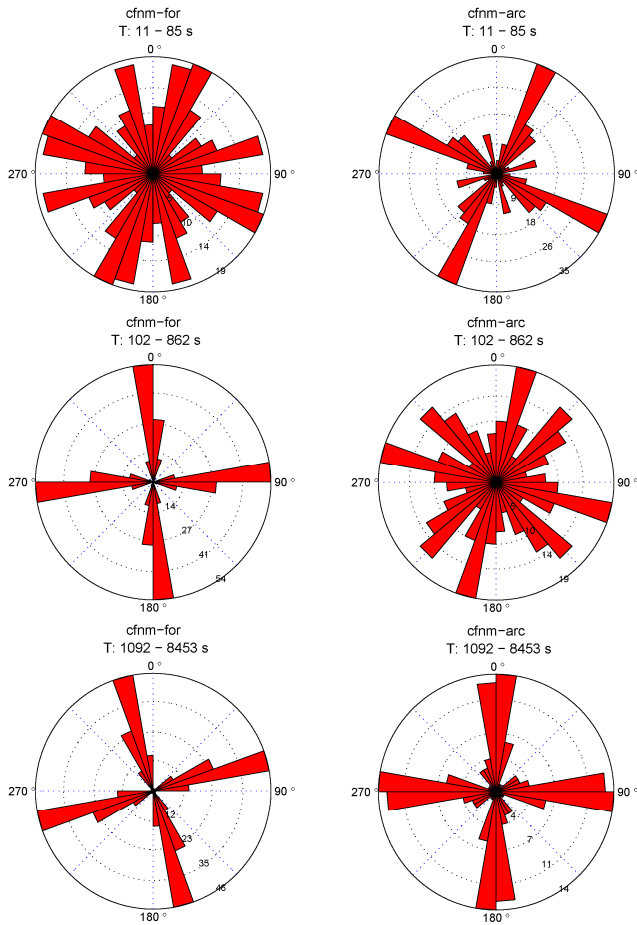


Figure S3. Rose histograms of impedance phase tensor ellipse principal axes over three period bands for the CAFE MT profile.

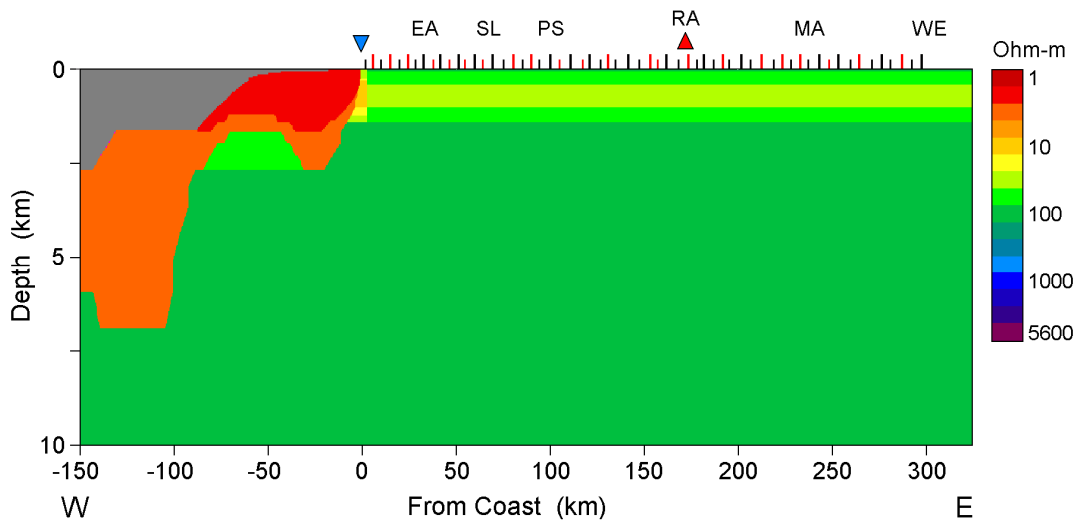


Figure S4. Upper 10 km of starting and a priori model for 2D inversion of the CAFE MT profile. Vertical exaggeration is 20:1.

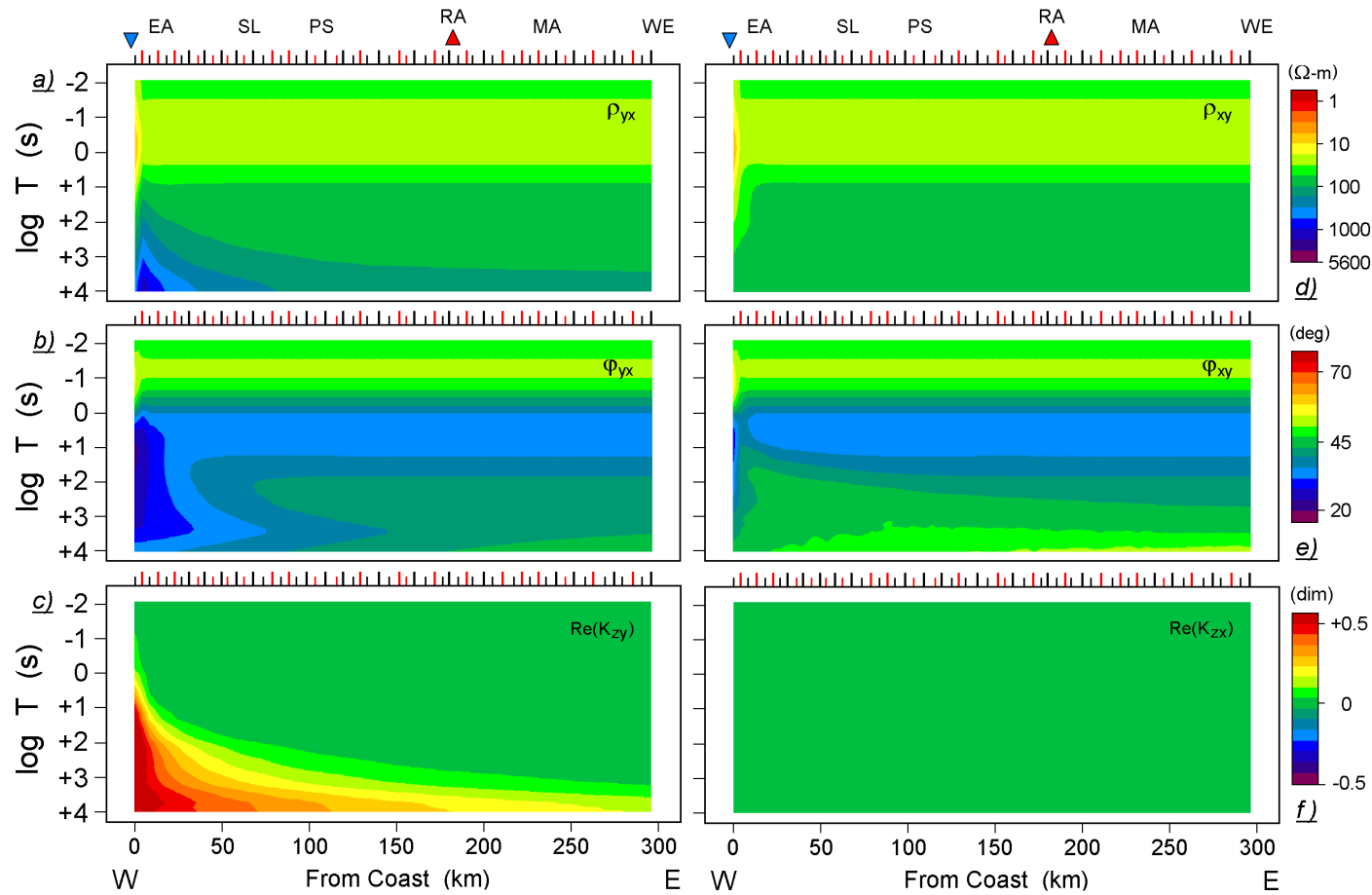


Figure S5. Left: Computed TM mode response in  $\rho_{yx}$  and  $\phi_{yx}$  plus  $\text{Re}(K_{zy})$  for the CAFE starting and a priori 2D inversion model. Right: Computed TE mode response in  $\rho_{xy}$  and  $\phi_{xy}$  for the CAFE starting and a priori 2D inversion model.  $\text{Re}(K_{zx})$  is zero in 2D.

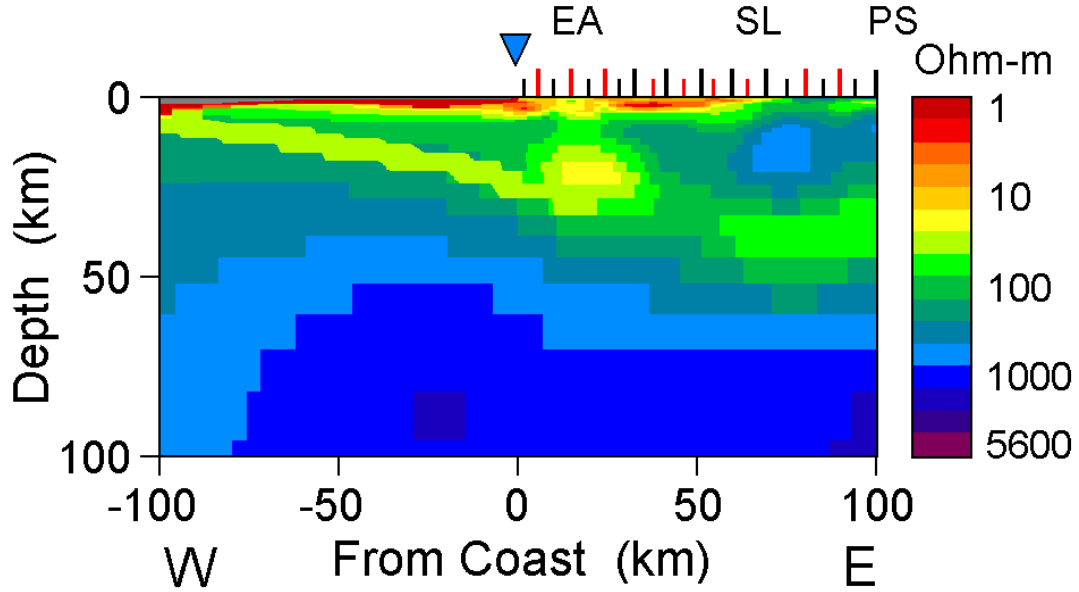


Figure S6. Test model of permissible conductance at plate interface below coastal area on the CAFE MT transect for inversion model of main text Figure 2 with thin dipping conductor imposed along plate interface. Plot shows layer of 25 ohm-m; layer of 12 ohm-m also considered.

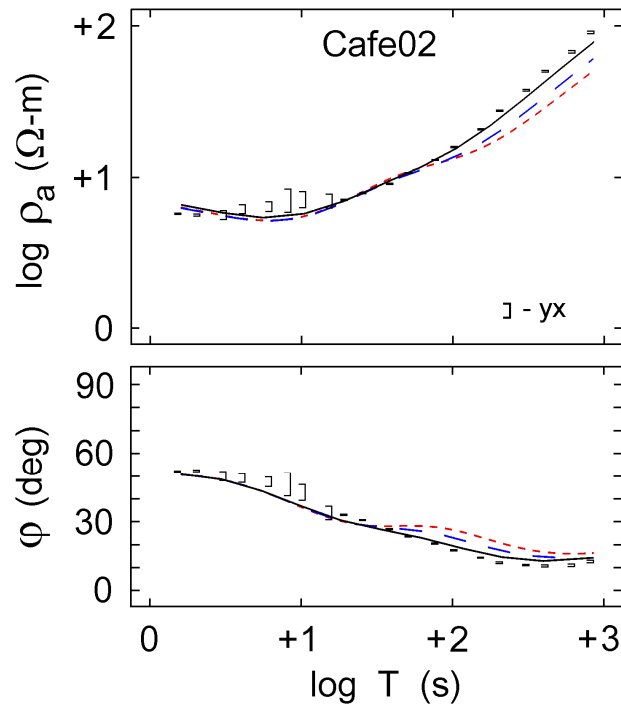


Figure S7. Observed data at second site in from coast plus computed responses of main text Figure 2 model, plus that model with 25 (long blue dashes) and 12 ohm-m (short red dashes) thin layers imposed.

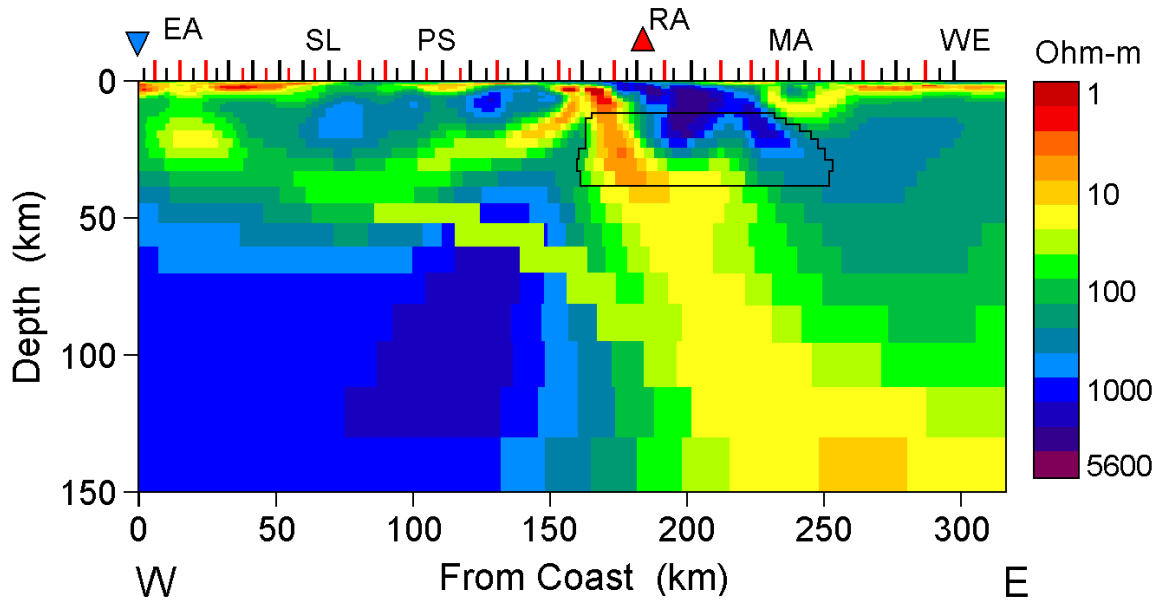


Figure S8. Test model of with thin conductor of 40 ohm-m resistivity corresponding to fluidized oceanic crust subducted to sub-arc depths beneath Mount Rainier on the CAFÉ transect. Black outlines polygon beneath Rainer denotes area fixed to 200 ohm-m in test of Figure S10 and S11.

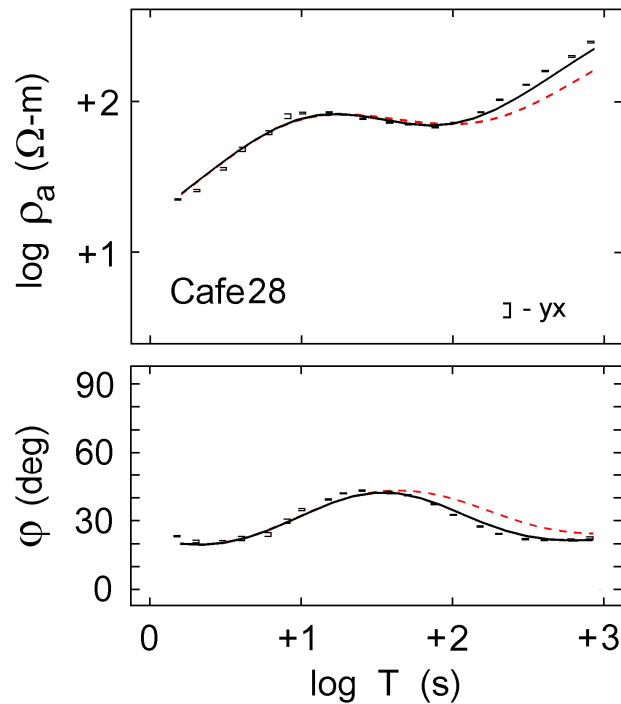


Figure S9. Observed data at site 28 in from coast plus computed responses of main text Figure 2 model, plus that model with 40 ohm-m (short red dashes) thin layer imposed along subducted oceanic crust as in Figure S8.

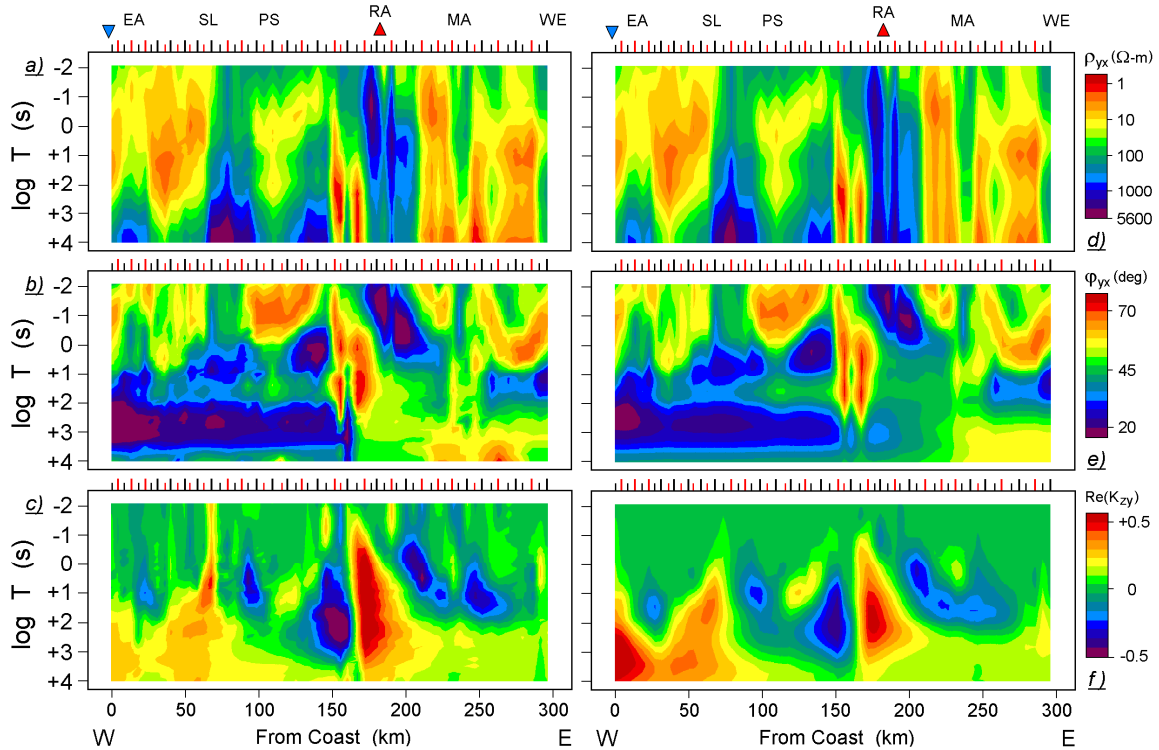


Figure S10. Left: Pseudosections of primary observed nominal MT quantities along the CAFE transect as defined in Figure S1. Right: Pseudosections of primary computed MT quantities along the CAFE transect from the best fit model of main text Figure 2 but with area under Mount Rainier fixed to 200 ohm-m as outlined in Figure S8.

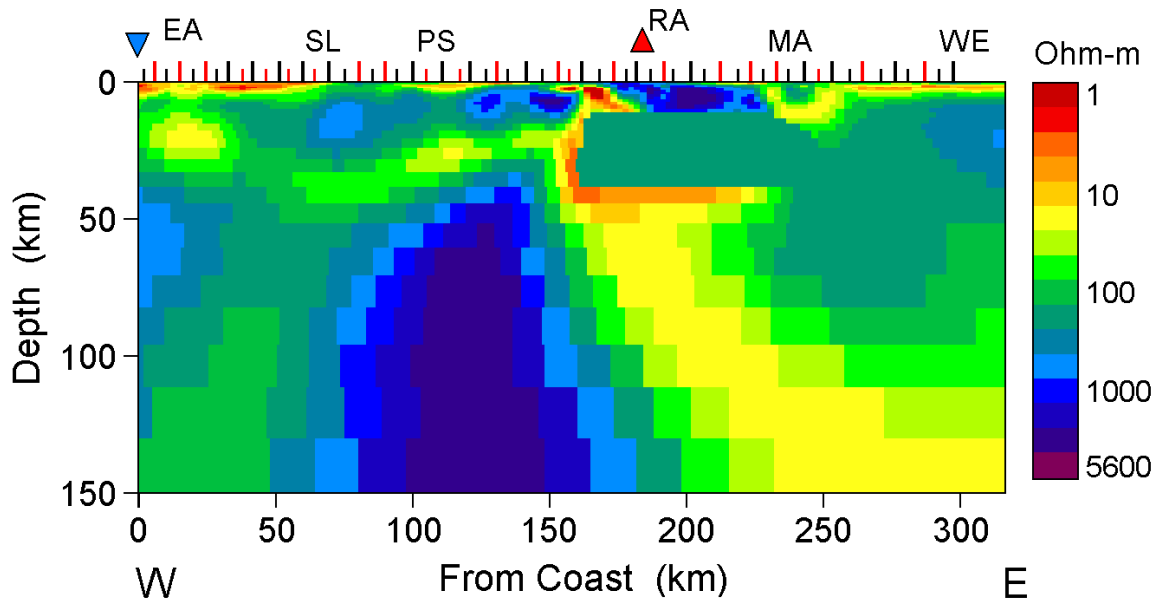


Figure S11. Inversion model for CAFE line when area under Mount Rainier denoted in Figure S8 is fixed to 200 ohm-m.

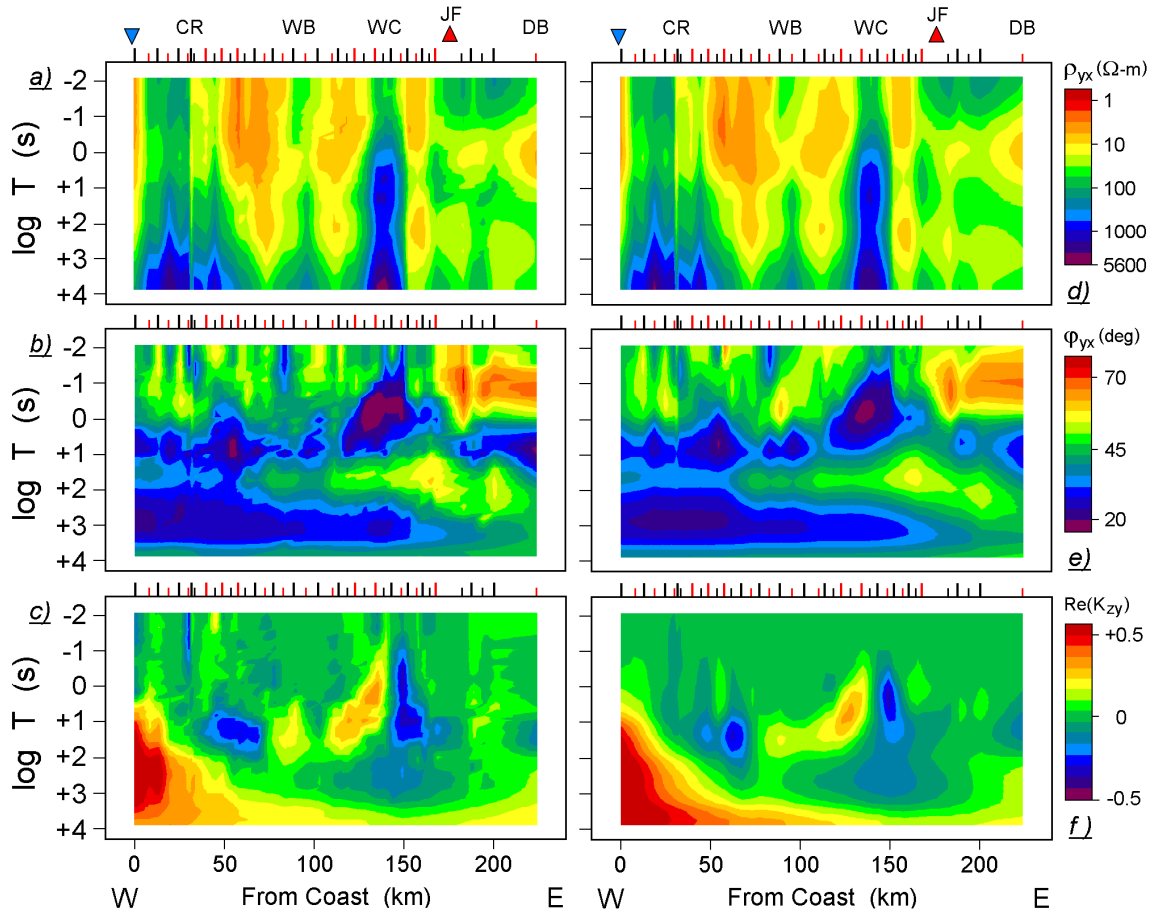


Figure S12. Left: Pseudosections of primary observed nominal MT quantities along the EMSLAB transect: (a), TM mode apparent resistivity  $\rho_{yx}$ ; (b), TM mode impedance phase  $\phi_{yx}$ ; (c), real component of TE mode normalized vertical magnetic field  $\text{Re}(K_{zy})$ . Units are logarithmically spaced ohm-m, linear degrees, and dimensionless. These observations are emphasized in the 2D inversion models. Right: Pseudosections of primary computed MT quantities along the EMSLAB transect from the model of main text Figure 3.

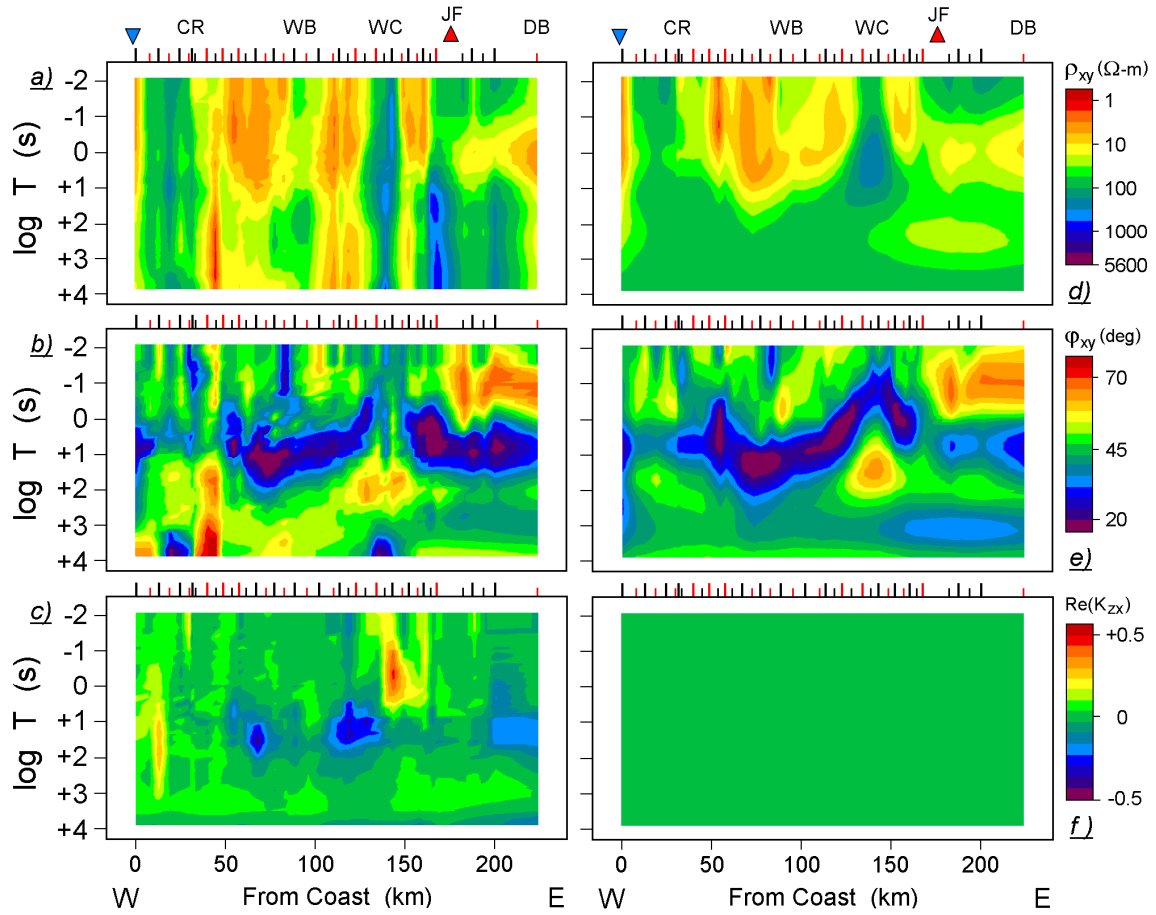
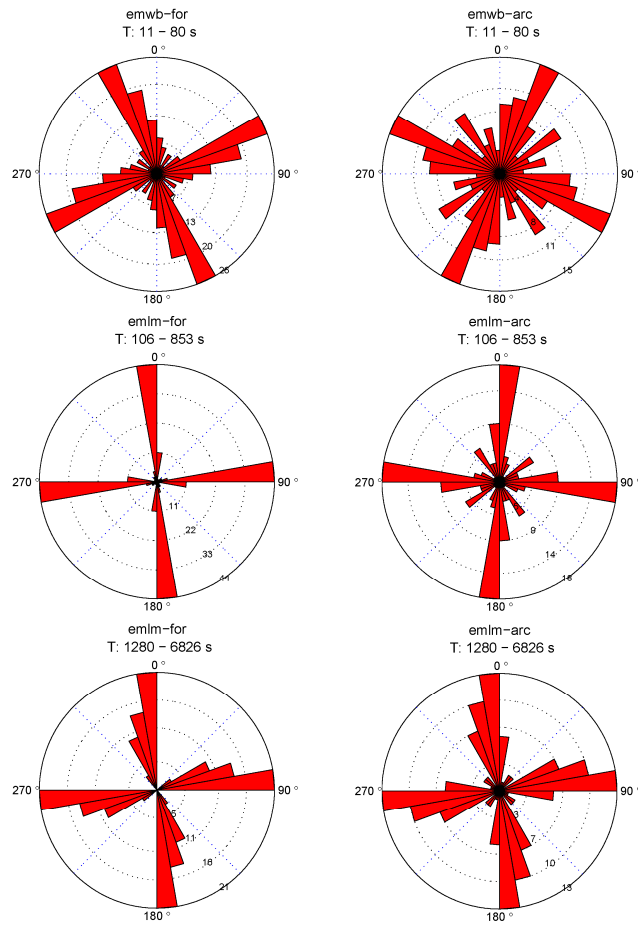


Figure S13. Left: Pseudosections of secondary observed MT quantities along the EMSLAB transect: (a), TE mode apparent resistivity  $\rho_{xy}$ ; (b), TE mode impedance phase  $\phi_{xy}$ ; (c), real component of TM mode normalized vertical magnetic field  $\text{Re}(K_{zx})$ . Units are logarithmically spaced ohm-m, linear degrees, and dimensionless. These observations are de-emphasized in the 2D inversion models. Right: Pseudosections of secondary computed MT quantities along the EMSLAB transect from the model of main text Figure 3.  $\text{Re}(K_{zx})$  is zero in 2D.



*Figure S14. Rose histograms of impedance phase tensor ellipse principal axes over three period bands for the EMSLAB profile.*

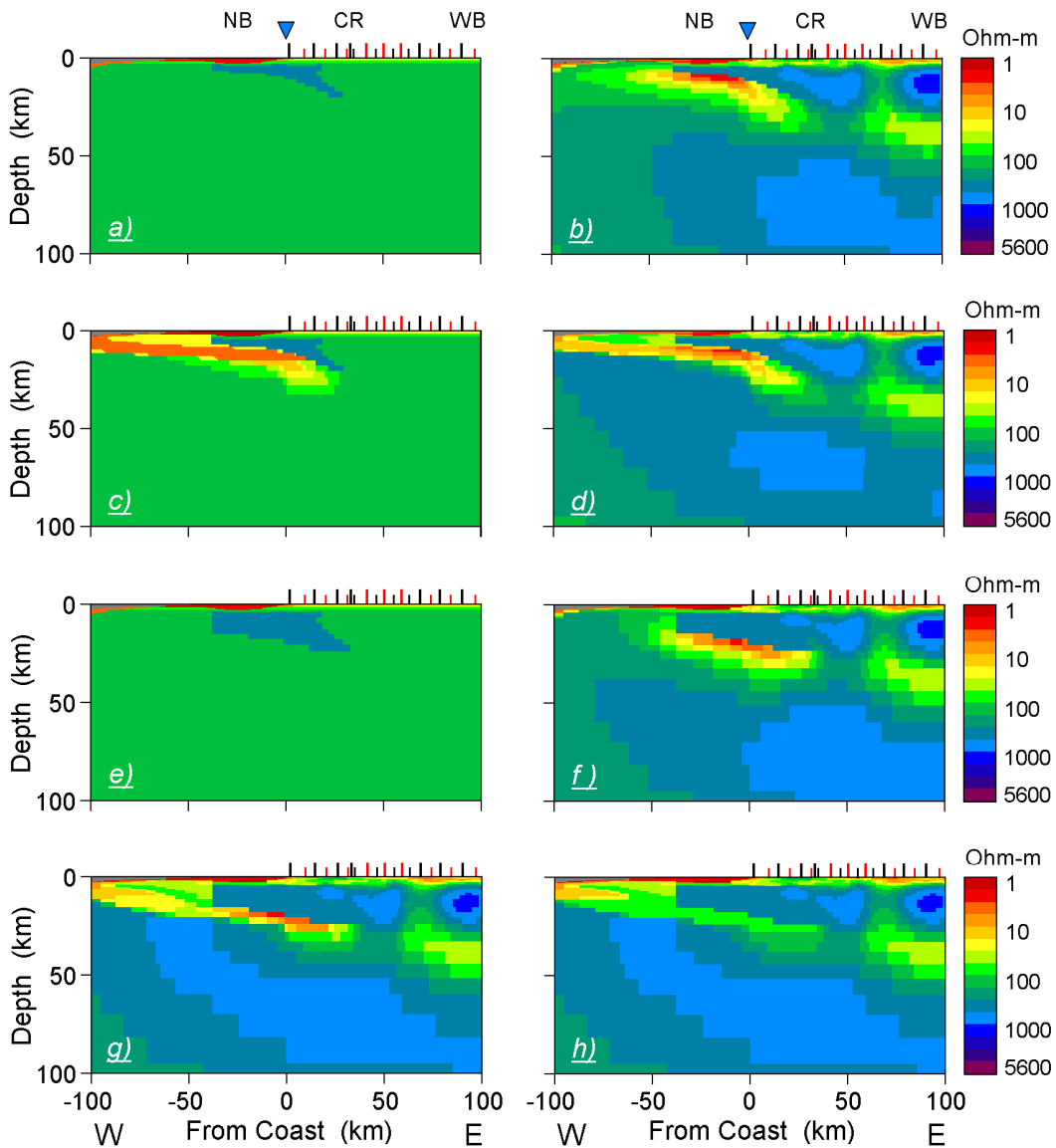


Figure S15. Test starting and inversion models aimed at exploring coast and shelf area structure of the EMSLAB line at the level of the plate interface and above: a), starting model with thin section of resistive Siletz terrane rocks imposed and fixed; b), inversion result with previous starting model; c), imposed Siletz material plus conductive interface in initial guess (but not fixed); d), inversion result with previous starting model; e), starting model with thick section of resistive Siletz terrane rocks imposed and fixed; f), inversion result with previous starting model; g), inversion result with imposed thick Siletz material plus conductive interface in initial guess (but not fixed); h), model with thin, weak interface conductor replacing inversion result of Figure S15g and forward response recomputed.

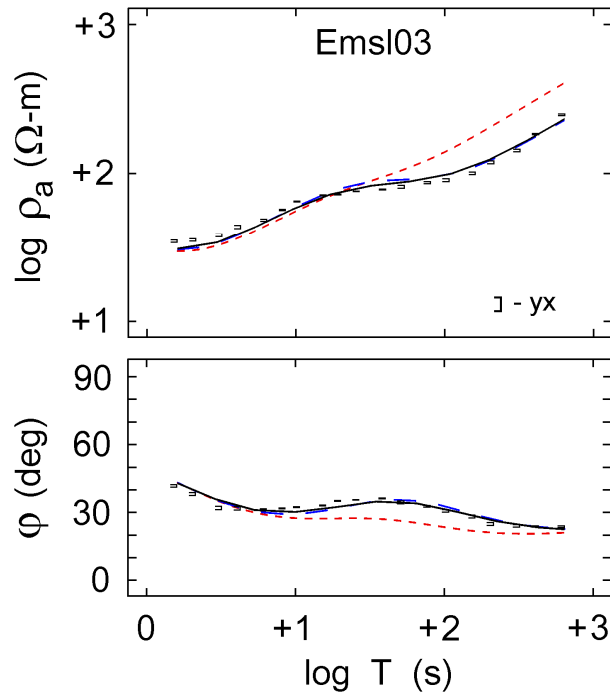


Figure S16. Observed TM mode data over middle period range for third EMSLAB site from the coast (14 km distance) together with computed response of inversion model of Figure 3 of main text (solid black line), computed response with thick Siletzia rocks imposed (Figure S15f) (long blue dashes), and computed response with thin, low conductance layer replacing strong conductor of inversion model of Figure S15h (thin red dashes).

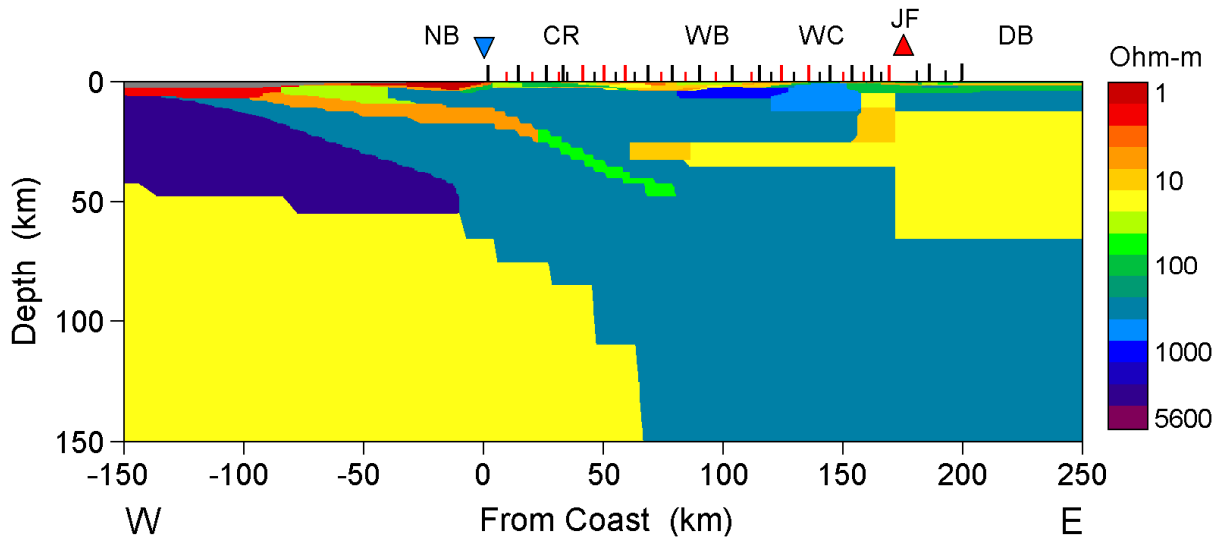


Figure S17. Legacy forward model of Wannamaker et al. (1989) plotted in color scheme consistent with other models of this paper.

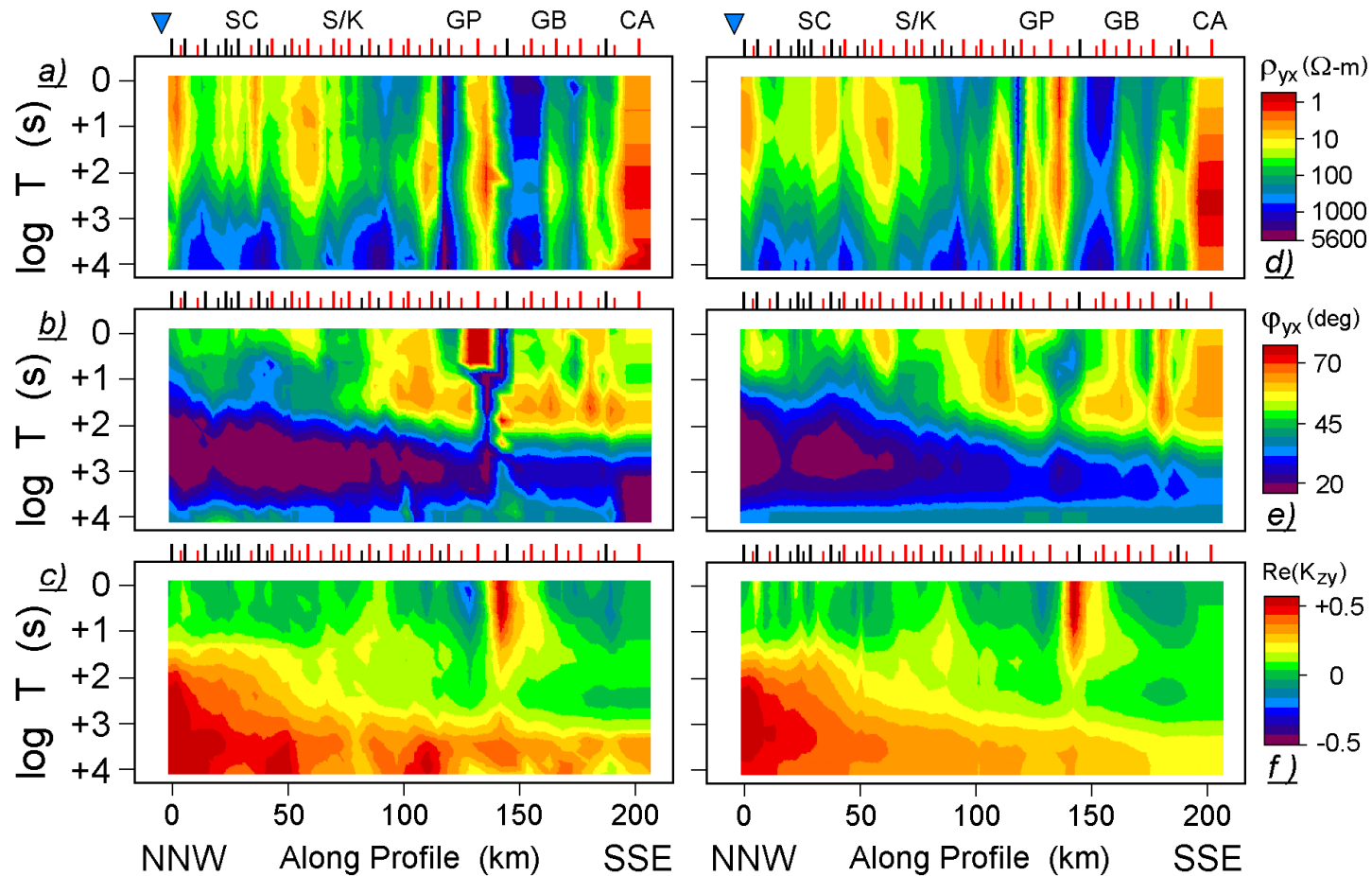


Figure S18. Left: Pseudosections of observed MT quantities along the SWORMT transect: (a), Apparent resistivity  $\rho_{yx}$ ; (b), Impedance phase  $\phi_{yx}$ ; (c), real component normalized vertical magnetic field  $\text{Re}(K_{zy})$ . The x-axis is north and y-axis is east as on other U.S. profiles, but modes are not assigned for the 3D interpretation. However, this would be the data subset to inspect for presence of plate interface phase peak, which is absent in this case. Units are logarithmically spaced ohm-m, linear degrees, and dimensionless. Right: Pseudosections of computed MT quantities along the SWORMT transect from the model of main text Figure 4.

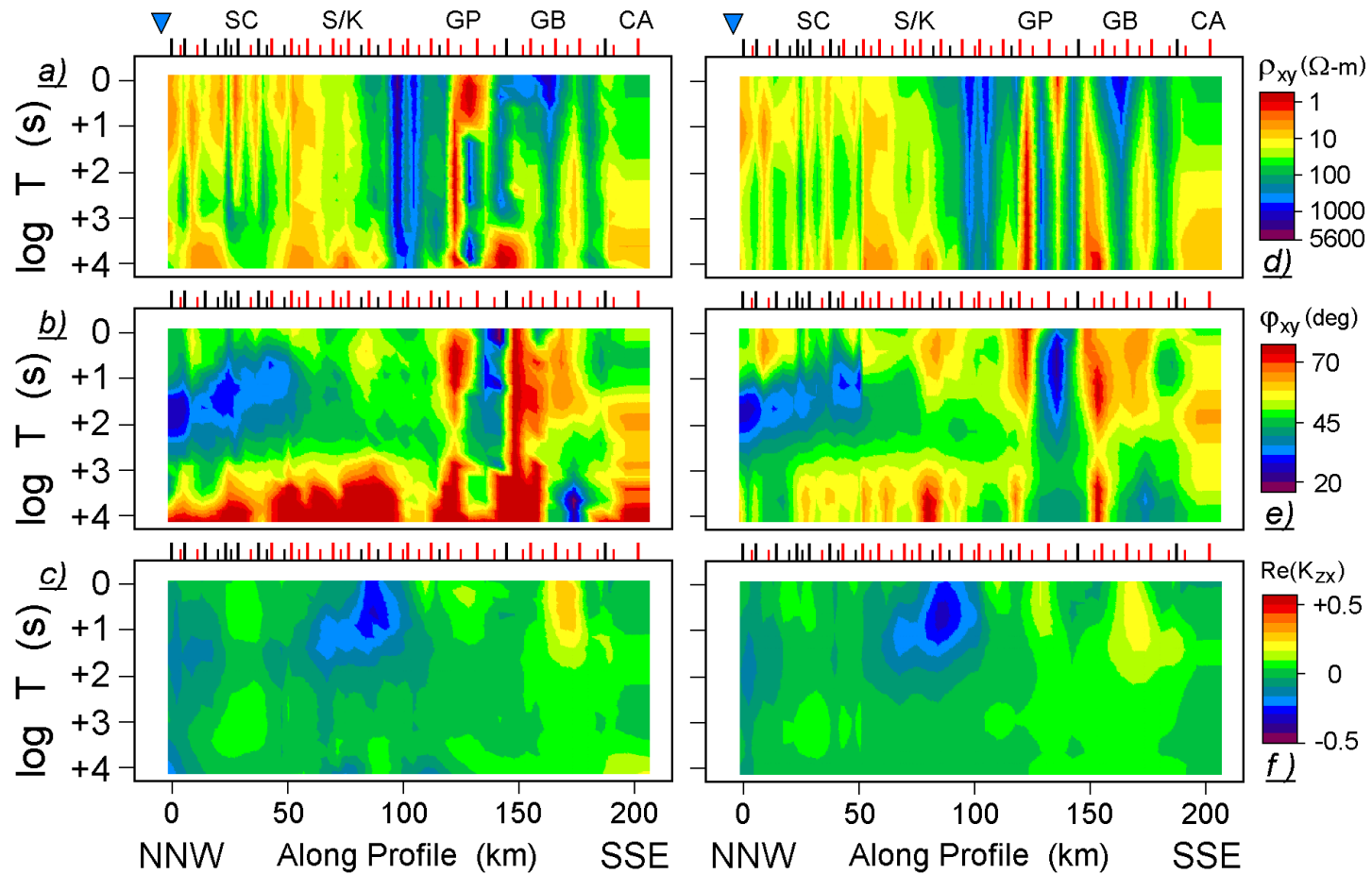


Figure S19. Left: Pseudosections of observed MT quantities along the SWORMT transect: (a), Apparent resistivity  $\rho_{xy}$ ; (b), Impedance phase  $\phi_{xy}$ ; (c), real component normalized vertical magnetic field  $Re(K_{zx})$ . The x-axis is north and y-axis is east as on other U.S. profiles, but modes are not assigned for the 3D interpretation. Units are logarithmically spaced ohm-m, linear degrees, and dimensionless. Right: Pseudosections of computed MT quantities along the SWORMT transect from the model of main text Figure 4.

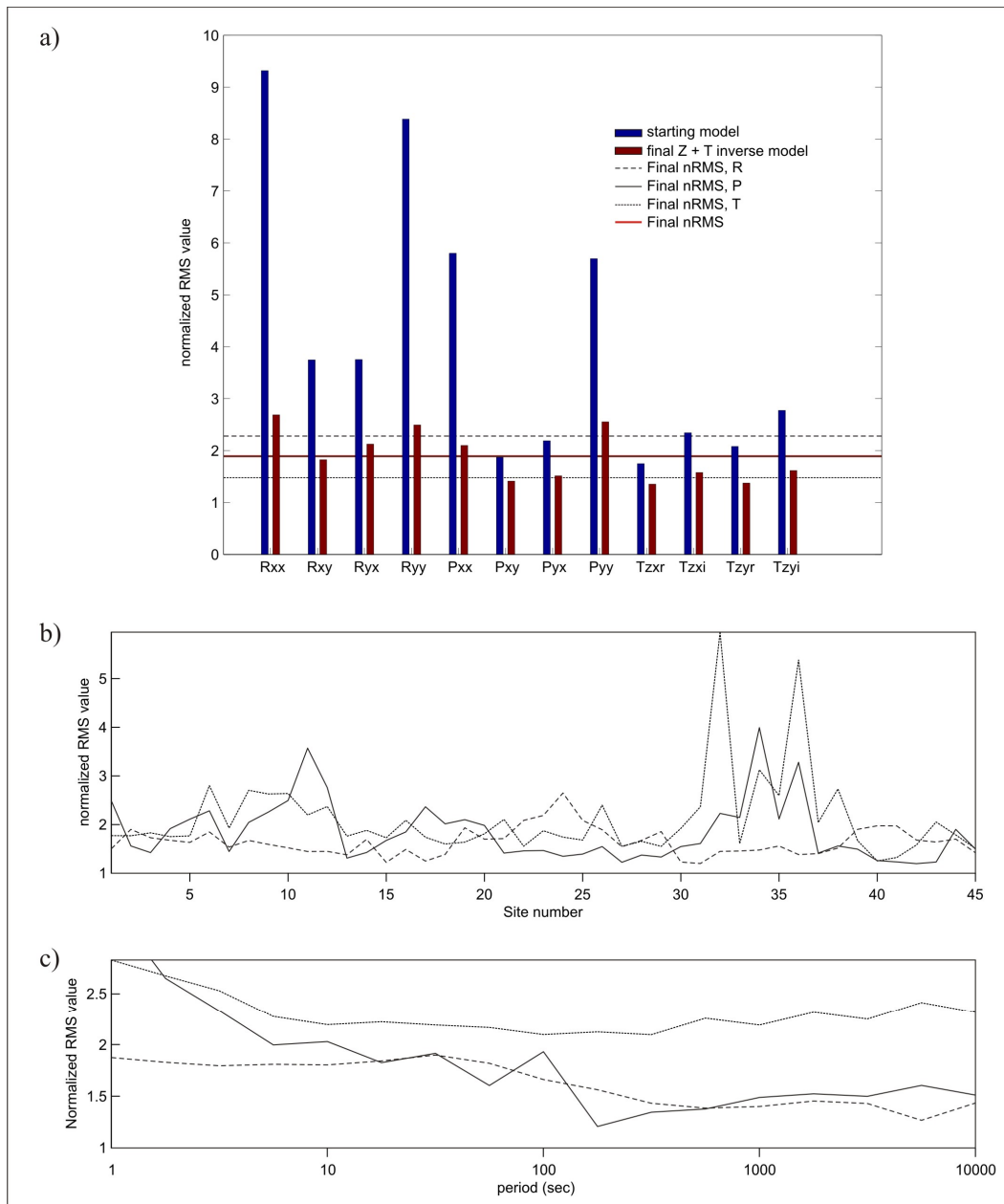


Figure S20. Misfit of starting and final 3D model arrayed by MT data component.

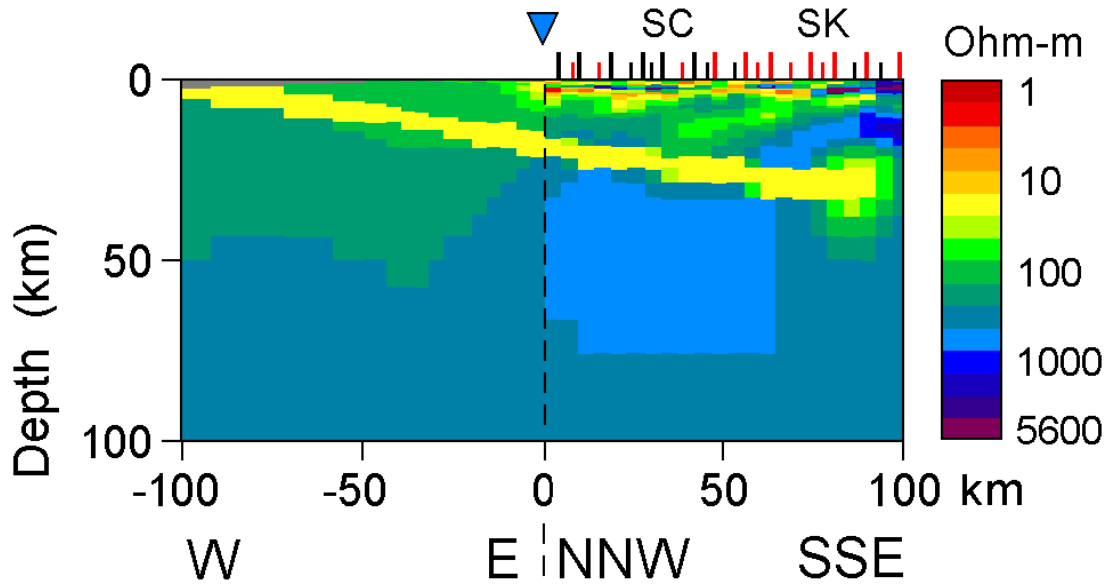


Figure S21. View of test conductive layer inserted along the plate interface region in the overall 3D inversion model of the SWORMT data set. Depicted here is the 12 ohm-m layer; a 25 ohm-m layer was tested as well. Vertical dashed line denotes bend in section at coast

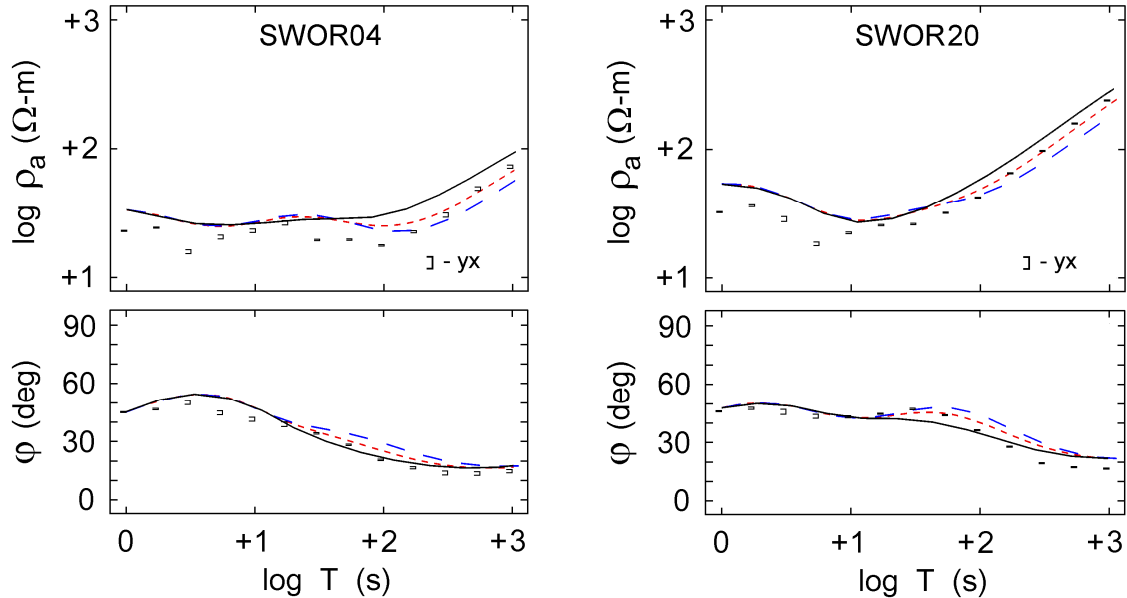


Figure S22. Measured responses at two sites 8 and 65 km along the SWORMT profile from the coast (third and eighteenth sites) together with computations of preferred 3D inversion model of main text Figure 4 (solid black curves), the 25 ohm-m layer extending under the distal forearc (short red dashes) and the 12 ohm-m layer extending (long blue dashes).

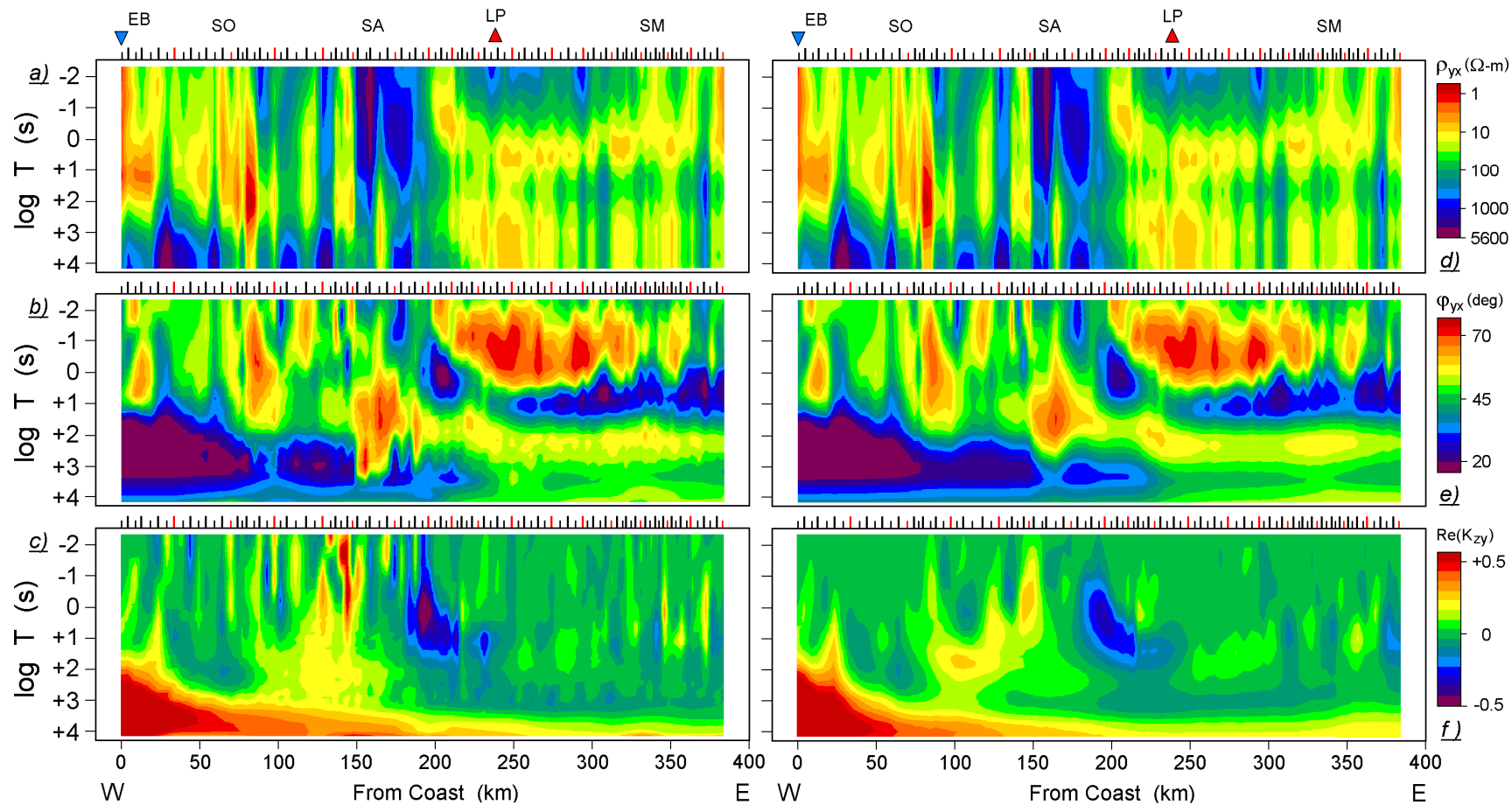


Figure S23. Left: Pseudosections of primary observed nominal MT quantities along the Klamath-Modoc transect: (a), TM mode apparent resistivity  $\rho_{yx}$ ; (b), TM mode impedance phase  $\phi_{yx}$ ; (c), real component of TE mode normalized vertical magnetic field  $\text{Re}(K_{zy})$ . Units are logarithmically spaced ohm-m, linear degrees, and dimensionless. These observations are emphasized in the 2D inversion models. Right: Pseudosections of primary computed MT quantities along the Klamath-Modoc transect from the model of main text Figure 5.

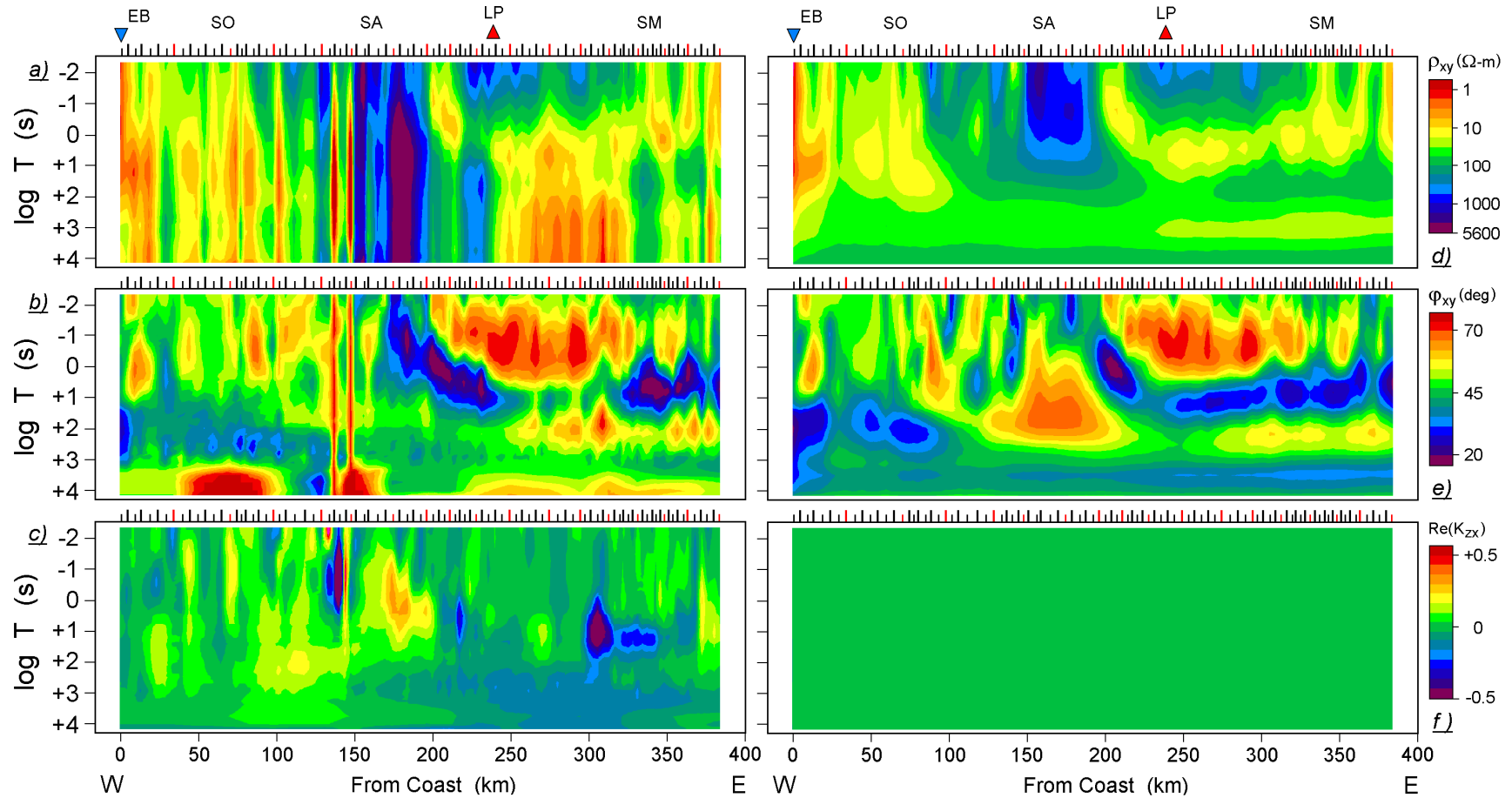


Figure S24. *Left:* Pseudosections of secondary observed MT quantities along the Klamath-Modoc transect: (a), TE mode apparent resistivity  $\rho_{xy}$ ; (b), TE mode impedance phase  $\phi_{xy}$ ; (c), real component of TM mode normalized vertical magnetic field  $\text{Re}(K_{zx})$ . Units are logarithmically spaced ohm-m, linear degrees, and dimensionless. These observations are de-emphasized in the 2D inversion models. *Right:* Pseudosections of secondary computed MT quantities along the Klamath-Modoc transect from the model of main text Figure 5.  $\text{Re}(K_{zx})$  is zero in 2D.

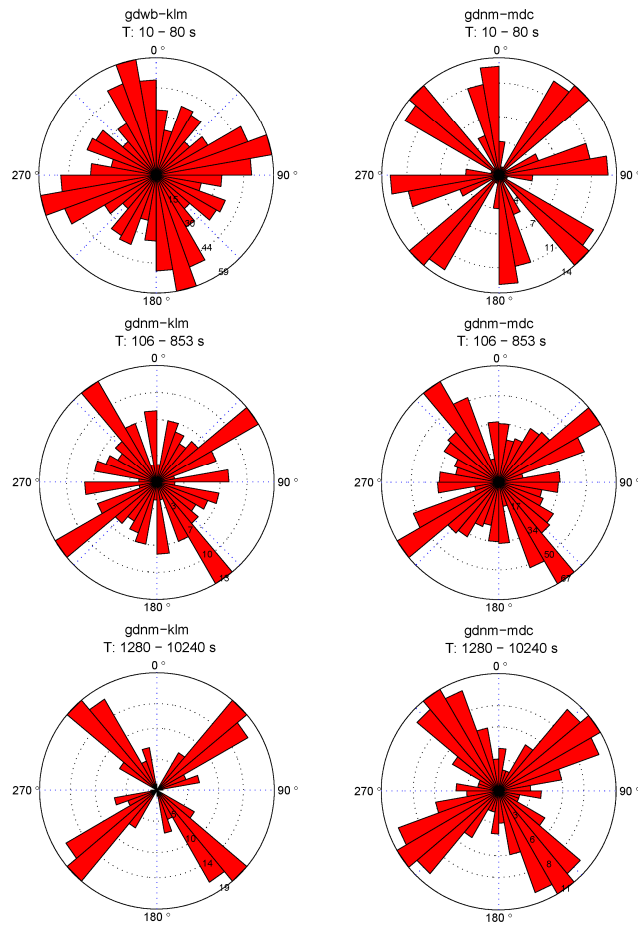


Figure S25. Rose histograms of impedance phase tensor ellipse principal axes over three period bands for the Klamath-Modoc profile.

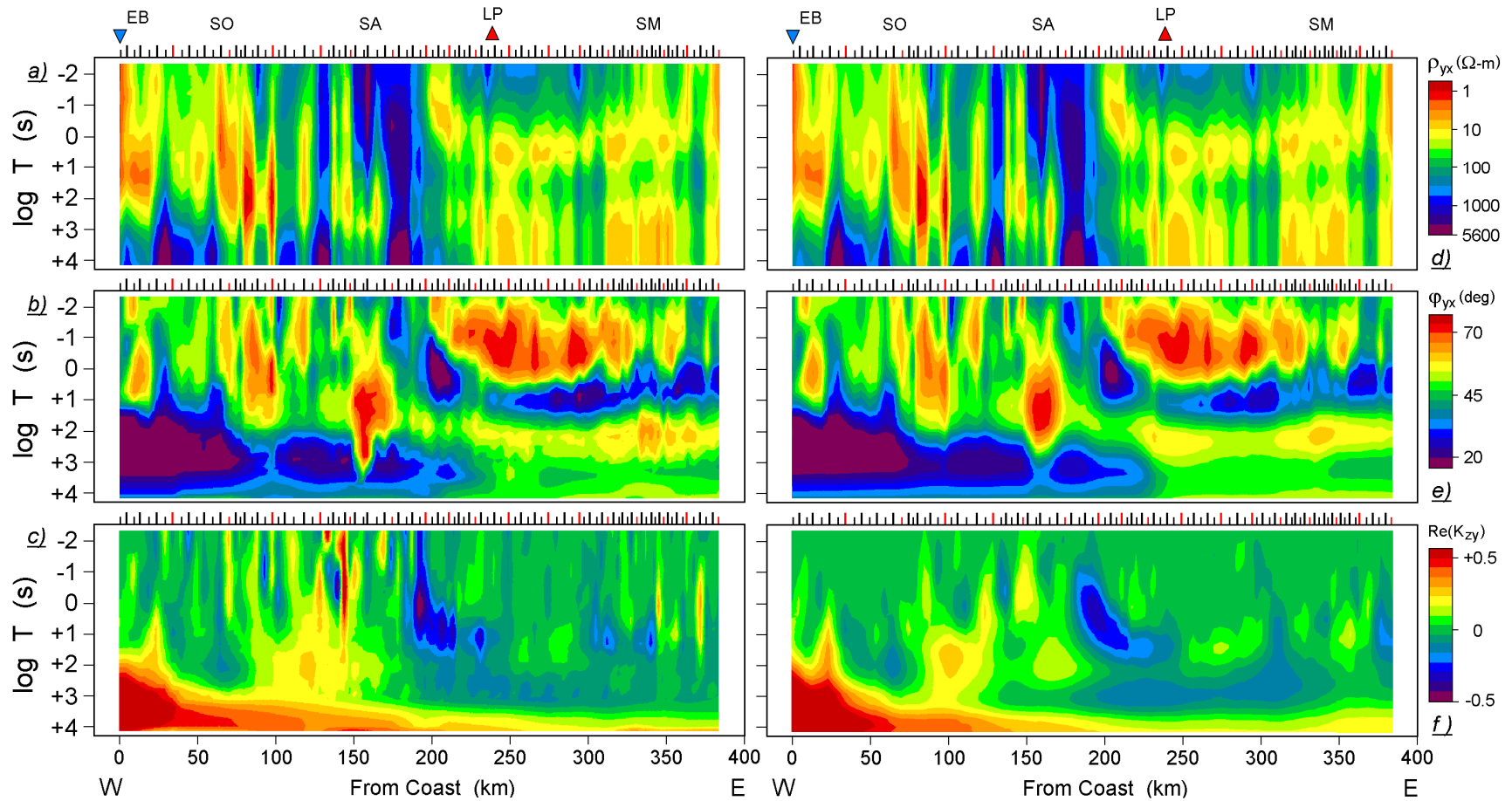


Figure S26. Pseudosections of primary observed MT quantities along the Klamath-Modoc transect for  $x=N025W$ : (top), TM mode apparent resistivity  $\rho_{yx}$ ; (middle), TM mode impedance phase  $\phi_{yx}$ ; (bottom), real component of TE mode normalized vertical magnetic field  $\text{Re}(K_{zy})$ . Units are logarithmically spaced ohm-m, linear degrees, and dimensionless. These observations are emphasized in the 2D inversion model of Figure S28. Right: Pseudosections of primary computed MT quantities along the Klamath-Modoc transect from the model of Figure S28.

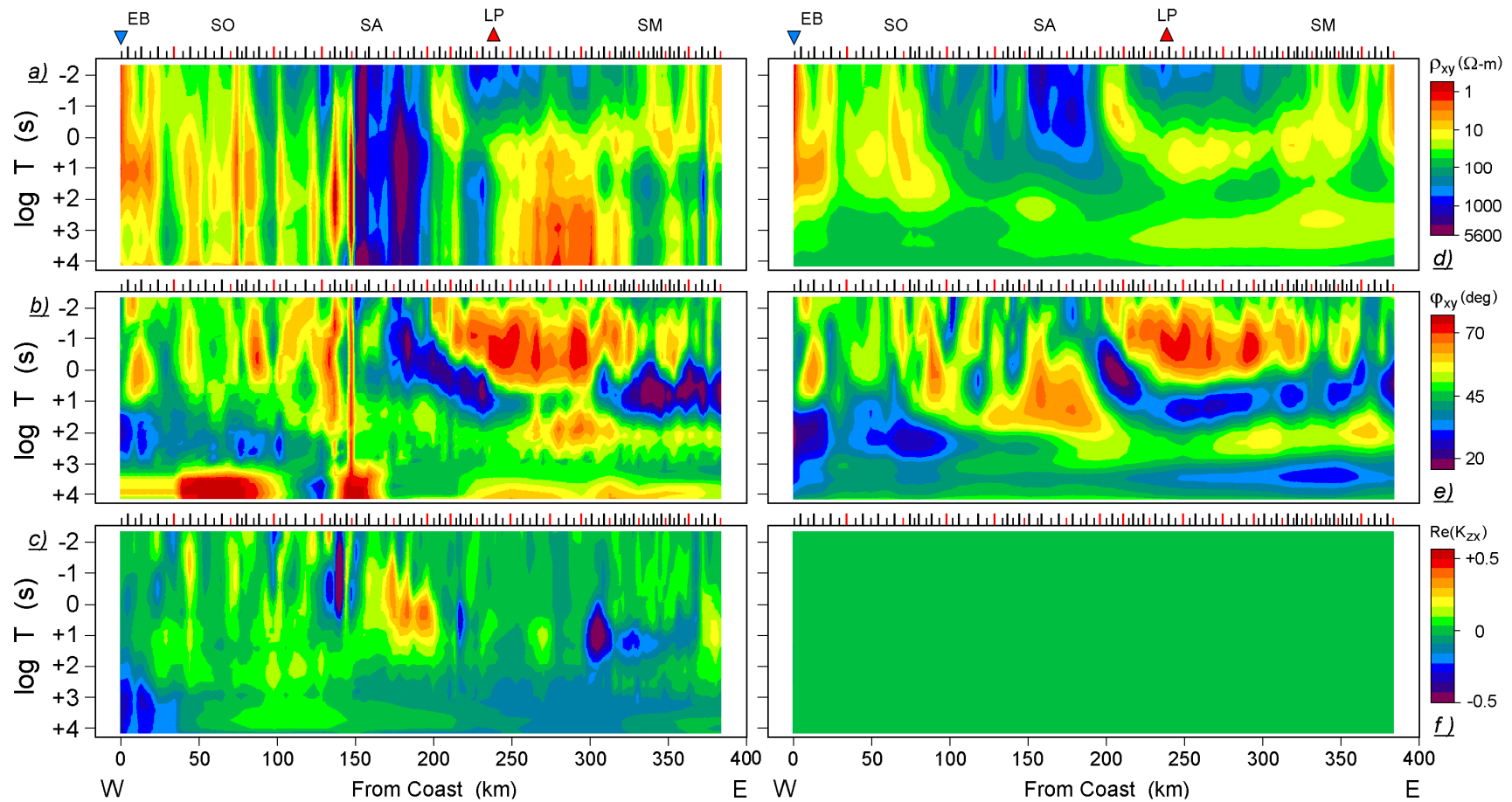


Figure S27. Pseudosections of secondary observed MT quantities along the Klamath-Modoc transect for  $x=N025W$ : (top), TE mode apparent resistivity  $\rho_{xy}$ ; (middle), TE mode impedance phase  $\phi_{xy}$ ; (bottom), real component of TM mode normalized vertical magnetic field  $Re(K_{zx})$ . Units are logarithmically spaced ohm-m, linear degrees, and dimensionless. These observations are de-emphasized in the 2D inversion of Figure S28. Right: Pseudosections of secondary computed MT quantities along the Klamath-Modoc transect from the model of Figure S28.

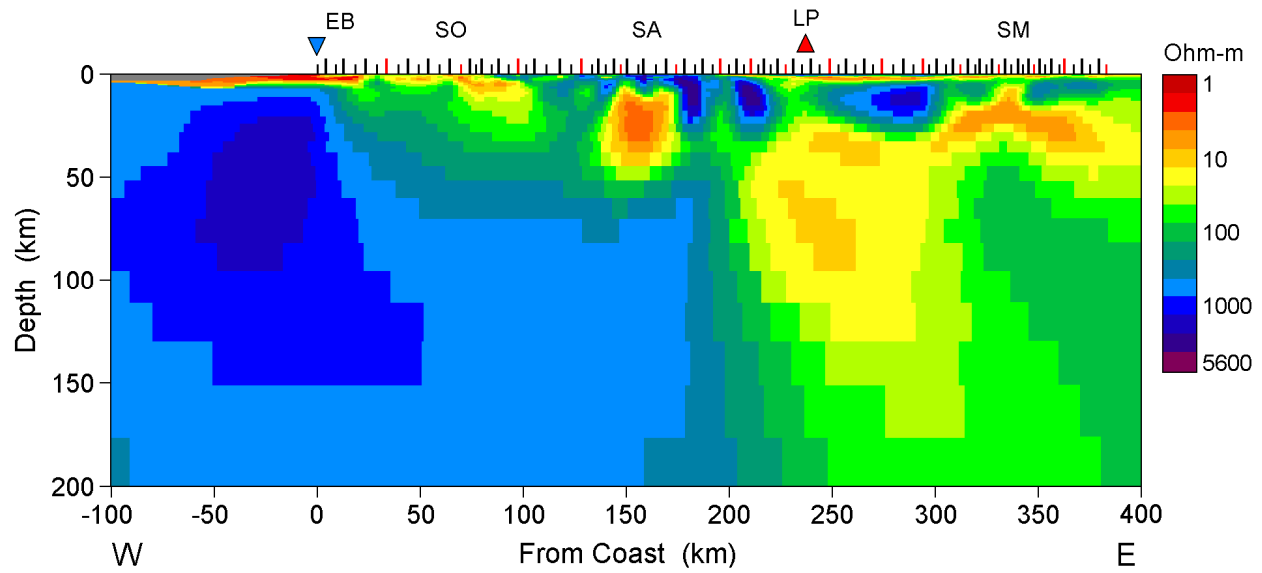


Figure S28. Two-dimensional inverse model of Klamath-Modoc data when strike is defined as  $x=N025W$ , similar to the Park and Ostos (2013) analysis.

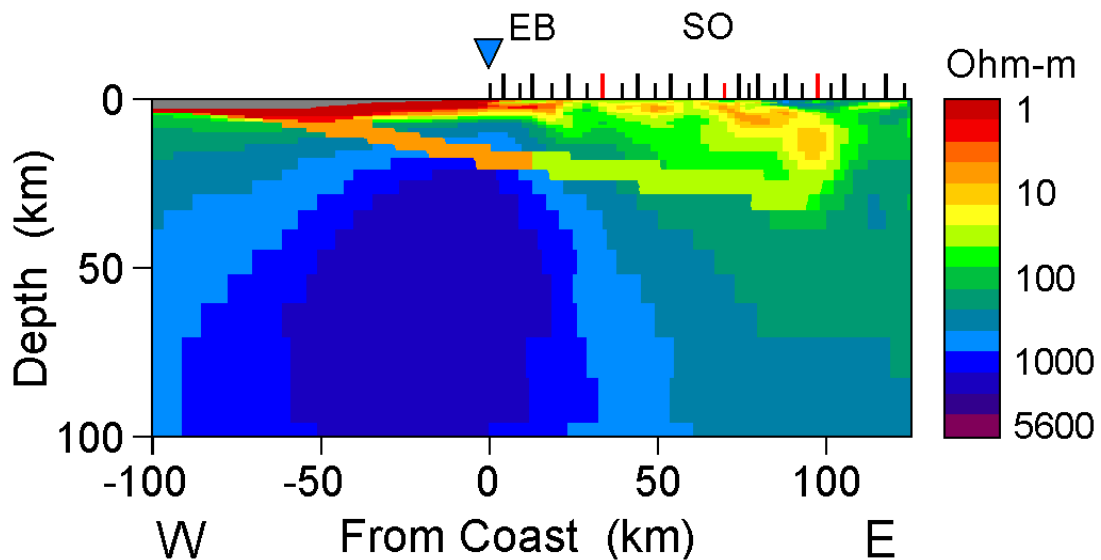


Figure S29. Models for the Klamath-Modoc profile testing permissible conductances along the plate interface near the coast.

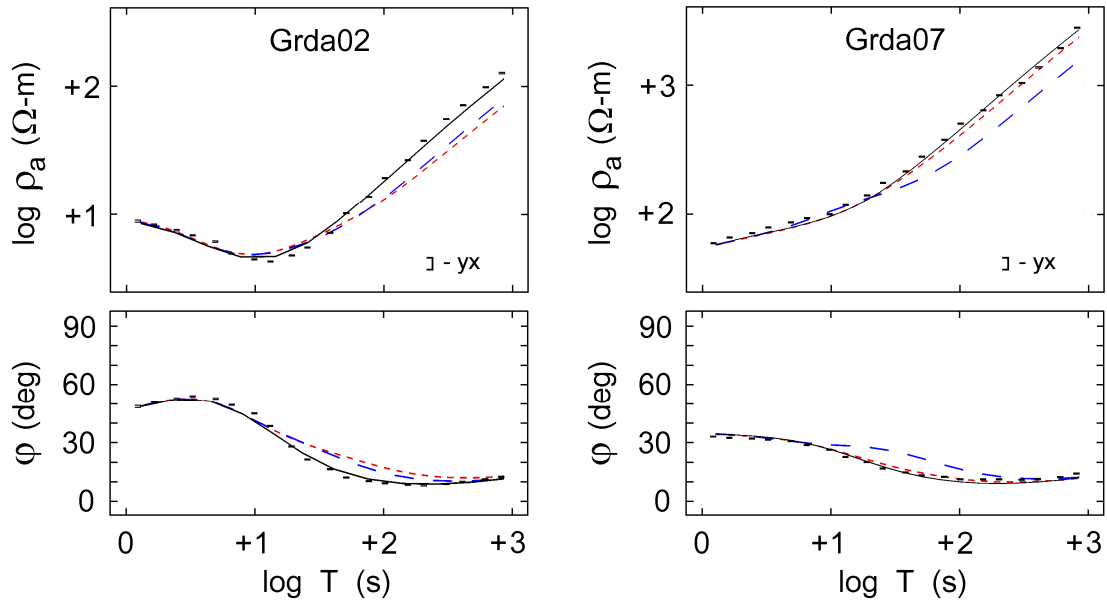


Figure S30. Measured responses at two sites 5 and 36 km from the shoreline (second and seventh sites) together with computations of preferred inversion model of main text Figure 5 and the lower conductance layer extending to under South Mountain (long blue dashes) and the high conductance but shorter layer terminating under the Eel River basin (short red dashes).

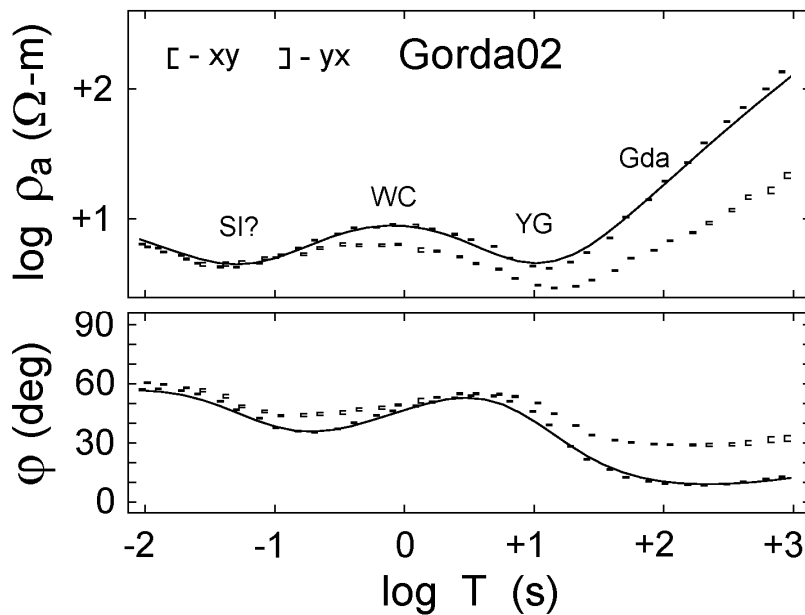


Figure S31. Second MT sounding located ~5 km from the shoreline on the Eel River delta. Double minimum in apparent resistivity denotes possible seawater incursion (SI?), then Yager Fm shales (YG) below Wildcat Group clastics (WC). Long period uptrend denotes wave penetration to resistive Gorda plate (Gda). A 2D model closeup is given in Figure 6 of main text.

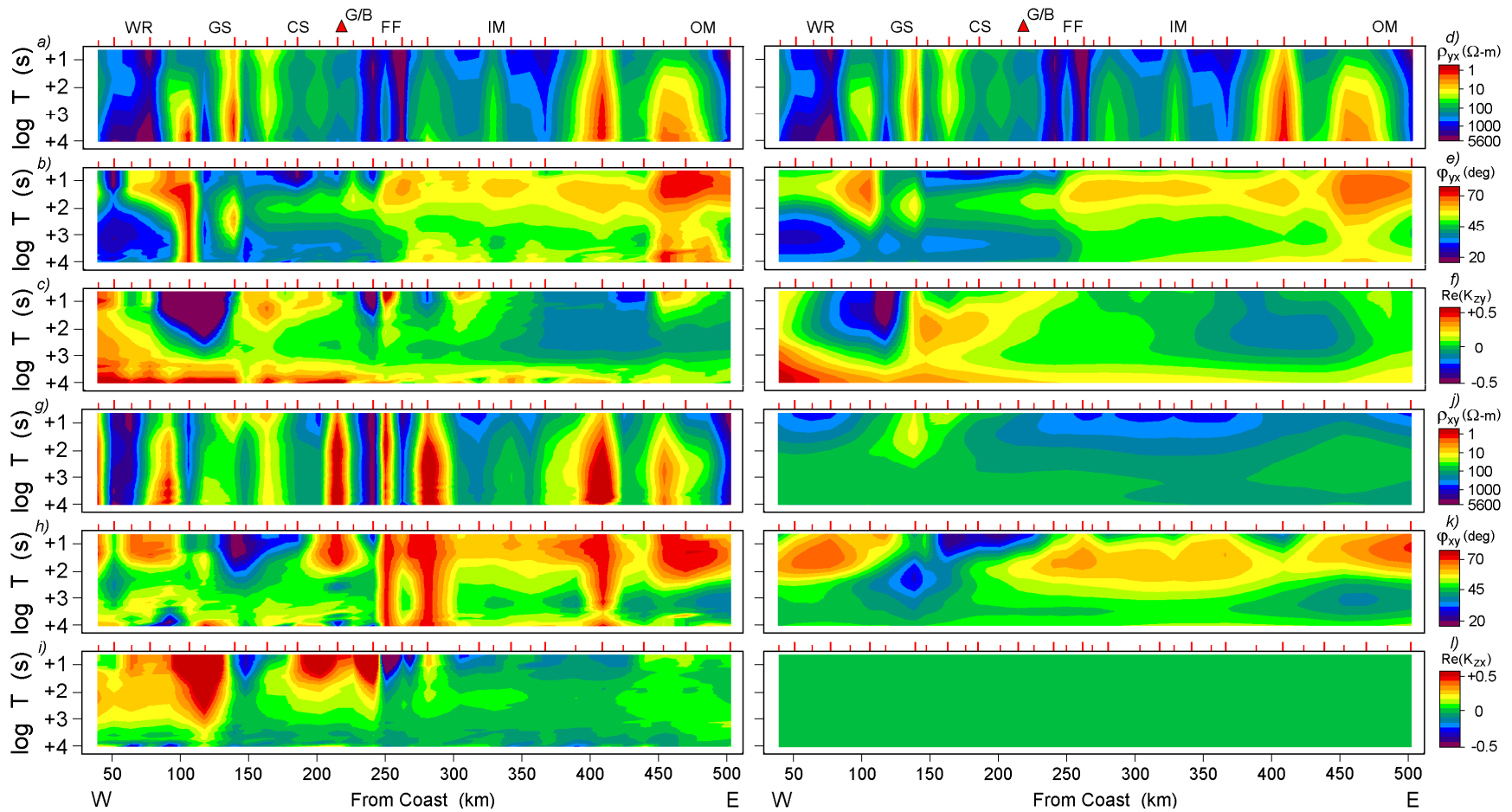


Figure S32. Left: Pseudosections of observed MT quantities along the ABCS transect: (a), nominal TM mode apparent resistivity  $\rho_{yx}$ ; (b), TM mode impedance phase  $\phi_{yx}$ ; (c), real component of TE mode normalized vertical magnetic field  $\text{Re}(K_{zy})$ ; (g), nominal TE mode apparent resistivity  $\rho_{xy}$ ; (h), TE mode impedance phase  $\phi_{xy}$ ; (i), real component of cross-strike normalized vertical magnetic field  $\text{Re}(K_{zx})$ . Units are logarithmically spaced ohm-m, linear degrees, and dimensionless. The first three panels are emphasized in the 2D inversion models. Right: Pseudosections of computed MT quantities along the ABCS transect from the model of main text Figure 7. Physiographic locations as in Figure 7.